

# NuGrid stellar data set – III. Updated low-mass AGB models and $s$ -process nucleosynthesis with metallicities $Z = 0.01$ , $Z = 0.02$ , and $Z = 0.03$

U. Battino,<sup>1</sup>★ A. Tattersall,<sup>1</sup> C. Lederer-Woods,<sup>1</sup> F. Herwig,<sup>2,3</sup> P. Denissenkov,<sup>2,3</sup>  
R. Hirschi,<sup>4,5</sup> R. Trappitsch,<sup>6</sup> J. W. den Hartogh<sup>7</sup> and M. Pignatari<sup>3,7,8</sup>  
(The NuGrid Collaboration†)

<sup>1</sup>*School of Physics and Astronomy, University of Edinburgh, EH9 3FD, UK*

<sup>2</sup>*Department of Physics and Astronomy, University of Victoria, Victoria, BC V8P5C2, Canada*

<sup>3</sup>*Joint Institute for Nuclear Astrophysics - Center for the Evolution of the Elements, East Lansing, 48823, USA*

<sup>4</sup>*Astrophysics group, Lennard-Jones Laboratories, Keele University, Staffordshire ST5 5BG, UK*

<sup>5</sup>*Kavli IPMU (WPI), The University of Tokyo, Kashiwa, Chiba 277-8583, Japan*

<sup>6</sup>*Nuclear and Chemical Sciences Division, Lawrence Livermore National Laboratory, Livermore, CA 94551, USA*

<sup>7</sup>*Konkoly Observatory, Research Centre for Astronomy and Earth Sciences, Hungarian Academy of Sciences, Konkoly Thege M. t 15-17, 1121 Budapest, Hungary*

<sup>8</sup>*E.A. Milne Centre for Astrophysics, Department of Physics and Mathematics, University of Hull, Hull HU6 7RX, UK*

Accepted 2019 July 31. Received 2019 July 29; in original form 2019 June 6

## ABSTRACT

The production of the neutron-capture isotopes beyond iron that we observe today in the Solar system is the result of the combined contribution of the  $r$ -process, the  $s$ -process, and possibly the  $i$ -process. Low-mass asymptotic giant branch (AGB) ( $1.5 < M/M_{\odot} < 3$ ) and massive ( $M > 10 M_{\odot}$ ) stars have been identified as the main site of the  $s$ -process. In this work we consider the evolution and nucleosynthesis of low-mass AGB stars. We provide an update of the NuGrid Set models, adopting the same general physics assumptions but using an updated convective-boundary-mixing model accounting for the contribution from internal gravity waves. The combined data set includes the initial masses  $M_{ZAMS}/M_{\odot} = 2, 3$  for  $Z = 0.03, 0.02, 0.01$ . These new models are computed with the MESA stellar code and the evolution is followed up to the end of the AGB phase. The nucleosynthesis was calculated for all isotopes in post-processing with the NuGrid `mpnp` code. The convective-boundary-mixing model leads to the formation of a  $^{13}\text{C}$ -pocket three times wider compared to the one obtained in the previous set of models, bringing the simulation results now in closer agreement with observations. Using these new models, we discuss the potential impact of other processes inducing mixing, like rotation, adopting parametric models compatible with theory and observations. Complete yield data tables, derived data products, and online analytic data access are provided.

**Key words:** stars: abundances – stars: evolution – stars: interiors.

## 1 INTRODUCTION

Around half of the elements beyond Fe are the result of  $s$ -process nucleosynthesis (‘slow’ neutron-capture process; Cameron 1957; Burbidge et al. 1957; Gallino et al. 1998) taking place in massive stars ( $M > 10 M_{\odot}$ ) and low-mass asymptotic giant branch (AGB)

stars ( $1.5 < M/M_{\odot} < 3$ ). In particular, low-mass AGB stars are the main site of the main  $s$ -process component (e.g. Gallino et al. 1998; Käppeler et al. 2011), i.e. the nucleosynthesis process mainly responsible for around half of the neutron-capture element abundances between Zr and Bi in the Solar system. The AGB phase starts when the star has exhausted both H and He in the centre, leaving an inert degenerate carbon–oxygen (CO-) core surrounded by a thin He-intershell and a H-burning shell where nuclear energy is released and the structure is maintained in equilibrium. These shells are surrounded by an extended H-rich convective envelope.

\* E-mail: [ubattino@gmail.com](mailto:ubattino@gmail.com)

† <http://www.nugridstars.org>

For the majority of the AGB lifetime, nuclear energy is released in the H-burning shell. At the same time He and other H-burning ashes are accumulated on the top of He-intershell underneath, until He-burning starts and thin-shell instability occurs (Kippenhahn & Weigert 1990), triggering a violent thermonuclear runaway known as thermal pulse (TP) at typical temperature around  $3 \times 10^8$  K, enough to activate the neutron release via  $^{22}\text{Ne}(\alpha, n)^{25}\text{Mg}$  with high density (about  $10^{11}$  neutrons  $\text{cm}^{-3}$ ) lasting a few years. In these conditions the neutron exposure (defined as the total neutron flux integrated over time) is low because of the very short time-scales, preventing the neutron-capture flow to feed anything beyond the Sr-peak, but leaving a clear fingerprint in the isotopic ratios around branching points (unstable nuclei whose lifetimes are comparable to the neutron-capture time-scale). An example is the production of  $^{96}\text{Zr}$ , which requires high neutron densities to trigger neutron captures on  $^{95}\text{Zr}$  that has a half-life of 64 d (Lugaro et al. 2014). The TP will develop a pulse-driven convective zone (PDCZ), which mixes in the whole intershell the neutron-capture isotopes just synthesized and causes the expansion of the outer convective envelope (Herwig 2005). The temperature in the outer layer of the expanding convective envelope will thus decrease and opacity increase, which will make the convective motions more efficient. This last fact has two main consequences: (1) C and heavy element-rich material from the intershell is mixed into the convective envelope and brought to the surface (this event is known as third dredge-up, hereafter TDU, Straniero et al. 1995; Herwig 2005); (2) p-capture reactions are triggered on the abundant  $^{12}\text{C}$  which will produce  $\sim 10^{-4} M_{\odot}$   $^{13}\text{C}$ -rich material at the top of the intershell, known as  $^{13}\text{C}$ -pocket. This represents the main neutron source for the *s*-process via the  $^{13}\text{C}(\alpha, n)^{16}\text{O}$  reaction (at typical intershell temperature  $T \sim 0.09$  GK) (Straniero et al. 1995; Gallino et al. 1998). For these reasons, the *s*-process is very sensitive to how convective boundaries and hence chemical mixing across them are described. Because of the about three times lower temperature compared to typical He-flash conditions, the *s*-process in the  $^{13}\text{C}$ -pocket is characterized by low neutron densities ( $N_n \sim 10^7 \text{ cm}^{-3}$ ), but lasts for several thousand years, achieving high neutron exposure and producing second (Ba-region) and third (Pb-region) elements (Herwig 2005).

Over the last 20 yr, many efforts were dedicated to clarify the mixing mechanism at the boundary between the convective envelope and the He-intershell responsible for the formation of the  $^{13}\text{C}$ -pocket. Herwig et al. (1997), guided by multi-D simulations by Freytag, Ludwig & Steffen (1996), proposed an exponentially decaying diffusion mixing operating during the TDU. Later on, Langer et al. (1999) investigated the impact of rotation-induced mixing, which was shown by Herwig, Langer & Lugaro (2003) to not produce a large enough  $^{13}\text{C}$ -pocket. Denissenkov & Tout (2003) proposed a model based on internal gravity waves (IGW) induced by the convective motion in the envelope. Moreover, Straniero, Gallino & Cristallo (2006) and Cristallo et al. (2009) proposed an advection scheme as an alternative to the diffusion scheme. Finally, Nucci & Busso (2014) suggested magnetic buoyancy as a physical mechanism to transport H from the envelope into the He-C rich intershell.

Recently, Ritter et al. (2018) (hereafter RI18) computed a grid of stellar evolution and full-nucleosynthesis models over a wide range of both initial mass and metallicity, from 1 to 25  $M_{\odot}$ . The same stellar evolution code, post-processing code, and nuclear reaction network was adopted over the whole initial mass range, ensuring a high degree of internal consistency. The overshoot model by Herwig et al. (1997) and Herwig (2000) was adopted to describe

the convective-boundary-mixing (CBM) processes. This formed  $^{13}\text{C}$ -pockets producing a surface *s*-process enrichment between three and four times weaker than the highest abundances observed on C-stars (Busso et al. 2001; Abia et al. 2002; Zamora et al. 2009) and barium stars (Pereira et al. 2011; Cseh et al. 2018). This motivated Battino et al. (2016) to develop a new CBM prescription guided by the model proposed by Denissenkov & Tout (2003), and tested it at the bottom of the convective envelope during TDU episodes. The main result was a large increase of the pocket size up to around  $10^{-4} M_{\odot}$ .

In this work, we provide an update of the NuGrid data set presented in RI18, focusing on low-mass AGB models with initial metal content around solar value. In particular, we apply the same CBM model used by Battino et al. (2016) to RI18 models, keeping the other initial settings and stellar evolution code the same (MESA, revision 3709; see Paxton et al. 2010 for details) and using the post-processing nucleosynthesis code mppnp (Herwig et al. 2008; Pignatari et al. 2016). This work is organized as follows: in Section 2 we describe the stellar code and post-processing nucleosynthesis tools. In Section 3 the stellar models are presented, while in Section 4 we present our results, comparing them with a large set of observables. Our conclusions are given in Section 5.

## 2 COMPUTATIONAL METHODS

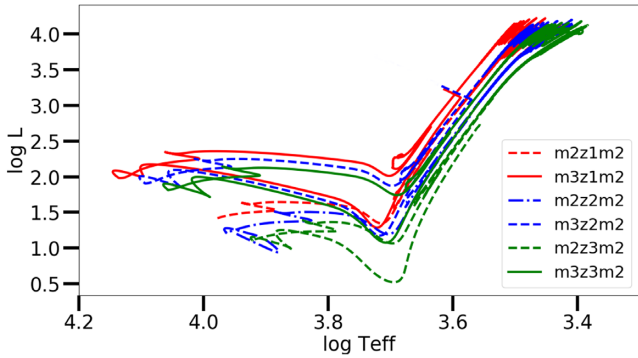
The stellar models presented in this section are computed using the stellar code MESA (revision 3709). We used the solar distribution from Grevesse & Noels (1993). The modelling assumptions are the same as in RI18, except we also computed  $Z = 0.03$  models. We adopted for  $Z = 0.03$  models the same modelling inputs as for  $Z = 0.02$  and  $Z = 0.01$  models, including, in order to stay consistent with RI18, the same mass-loss formula (Bloeker 1995) and efficiency parameter  $\eta_R$  during the C-rich phase. After the TDU event that makes the surface C/O ratio larger than 1.15, we chose the  $\eta_R$  value only depending on the initial mass, being  $\eta_R = 0.04$  and  $\eta_R = 0.08$  for the 2 and 3  $M_{\odot}$  models, respectively. For the simulations the MESA nuclear network *agb.net* is used, including 18 isotopes from protons to  $^{22}\text{Ne}$  linked by nuclear-reactions as in RI18. Here we also included  $^{20}\text{Ne}$ ,  $^{24}\text{Mg}$ ,  $^{28}\text{Si}$ , and  $^{56}\text{Fe}$  in order to avoid mass-conservation issues at the beginning of the simulations, without linking them to the other isotopes with nuclear reactions. The CBM modelling is included the same way as in Battino et al. (2016). This point is discussed in more details in Section 3.1.

The post-processing code mppnp was used, which is described in detail in Pignatari et al. (2016). The stellar structure evolution data are computed and saved with MESA for all zones at all time steps, and then used as input and processed with mppnp. This means that the stellar structure and the full nucleosynthesis are computed separately, hence requiring less computing time and resources. Full nucleosynthesis simulations are obtained by using a post-processing code and the pre-calculated stellar structure. In order to maintain consistency between stellar and nucleosynthesis calculations, MESA and mppnp adopt the same nuclear reaction rates relevant for energy generation and therefore for the evolution of the star. The higher number of isotopes considered during the nucleosynthesis has negligible effects on the stellar structure, since the nuclear reaction network used for MESA simulations already include all reactions relevant for nuclear energy generation.

The network is the same as in RI18. Exceptions relevant for this work are the neutron-capture cross-sections of  $^{90, 91, 92, 93, 94, 95, 96}\text{Zr}$ , for which we adopted rates recommended by Lugaro et al. (2014), based on recent experimental measurements (Tagliente et al. 2012).

**Table 1.** Main properties of the low-mass AGB models: initial mass, initial metallicity, H-free core mass at the beginning and the end of the AGB phase, and total lifetime are given. Core masses and total lifetimes obtained in **RI18** for models with same mass/metallicity combinations are also presented.

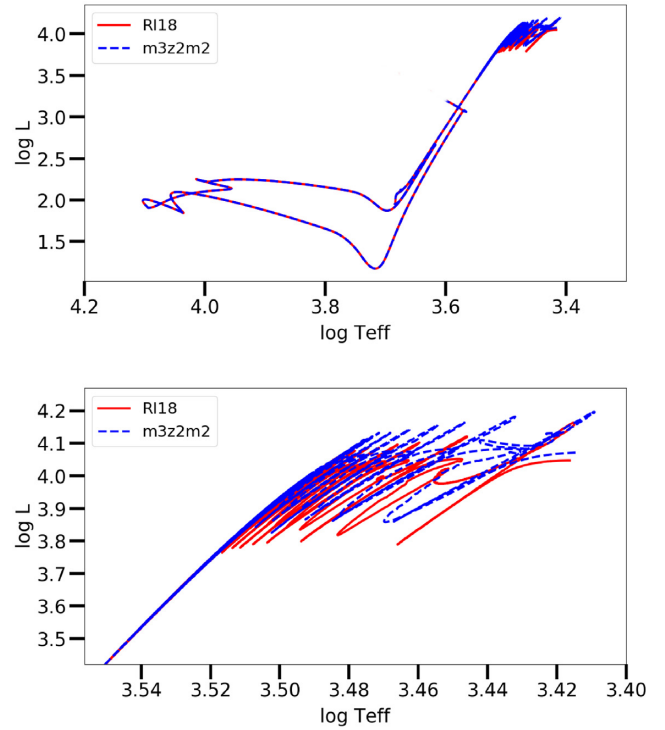
Name	$M_{\text{ini}} [M_{\odot}]$	$Z_{\text{ini}}$	H-free $M_{\text{ini}} [M_{\odot}]$	H-free $M_{\text{end}} [M_{\odot}]$	$\tau_{\text{tot}} [\text{yr}]$	H-free $M_{\text{ini}}$ <b>RI18</b>	H-free $M_{\text{end}}$ <b>RI18</b> [ $M_{\odot}$ ]	$\tau_{\text{tot}}$ <b>RI18</b>
m2z1m2	2	0.01	0.500	0.632	$1.28 \times 10^9$	0.498	0.617	$1.28 \times 10^9$
m3z1m2	3	0.01	0.641	0.661	$4.13 \times 10^8$	0.646	0.659	$4.13 \times 10^8$
m2z2m2	2	0.02	0.508	0.646	$1.40 \times 10^9$	0.510	0.620	$1.42 \times 10^9$
m3z2m2	3	0.02	0.598	0.656	$4.85 \times 10^8$	0.596	0.642	$4.82 \times 10^9$
m2z3m2	2	0.03	0.512	0.643	$1.71 \times 10^9$	–	–	–
m3z3m2	3	0.03	0.562	0.650	$6.03 \times 10^8$	–	–	–

**Figure 1.** HR diagram of tracks from all models listed in Table 1 from the pre-main-sequence to the tip of the AGB phase.

### 3 DESCRIPTION OF THE STELLAR MODELS

Table 1 lists the six stellar models calculated in this work, corresponding to three different initial metallicities ( $Z = 0.01$ ,  $Z = 0.02$ , and  $Z = 0.03$ ) and two initial masses ( $M = 2, 3 M_{\odot}$ ). All models' name start with an 'm' followed by a number indicating the initial mass in solar masses. After this, initial metallicity is expressed by what follows 'z'. For example, considering m3z2m2 'm3' means that this is a  $3 M_{\odot}$  model, 'z2m2' is to be read as  $Z = 2 \times 10^{-2}$ , where 'm2' means 'minus two' referring to the exponent. Key global features like core masses and lifetimes are given for all the models, which have all been computed with the same stellar code and input physics of **RI18**, but with the CBM model by Battino et al. (2016) during TDUs. This is why we also included the values from **RI18** in Table 1 (with the exception of  $Z = 0.03$  models which were not considered in **RI18**) and we compared our results to it all along this study.

Fig. 1 shows the HR diagram tracks from all the models listed in Table 1 from the pre-main-sequence to the tip of the AGB phase. Additionally, a comparison between HR diagrams of our m3z2m2 model and the corresponding one (same initial mass and metallicity) from **RI18** is given in Fig. 2. The two models are globally consistent along the evolution towards the AGB phase, where it is evident that the TP events experienced by the m3z2m2 model are more luminous than **RI18** by  $\text{Log}(L) \sim 0.7 L_{\odot}$ . Given the relation between core mass and luminosity during the AGB phase (Paczynski 1970), this is consistent with core masses listed in Table 1 being significantly larger than in **RI18**. The reason why the mass of the H-free core at the beginning of the TP-AGB is slightly different from **RI18** is due to a different choice of resolution details in the  $^{13}\text{C}$ -pocket formation region, just below the H-free core boundary. At the beginning of the TP-AGB phase, the application of the CBM model by Battino et al. (2016) requires a resolution down to around  $4 \times 10^{-6} M_{\odot}$ , more than a factor of two higher compared to  $10^{-5} M_{\odot}$  in **RI18**.

**Figure 2.** Upper panel: Comparison between HR diagrams of our m3z2m2 model and the corresponding one (same initial mass and metallicity) from **RI18**. Lower panel: Zoom on the AGB phase.

#### 3.1 The impact of different third-dredge-up efficiencies

The difference in core mass between **RI18** and this study is linked to the different CBM model here during TDUs. TDU affects the core-mass growth along the thermally pulsing AGB (TP-AGB) phase. We recall here that the efficiency of the TDU is usually expressed with

$$\lambda = (\delta M_{\text{DUP}} / \delta M_c) \quad (1)$$

defined as the fraction of the dredged-up mass ( $\delta M_{\text{DUP}}$ ) over the core-mass increment along an interpulse period ( $\delta M_c$ ). Every time a dredge-up episode takes place with an efficiency  $\lambda$ , the core mass decreases over the TDU duration by  $\lambda \delta M_c$  (see Marigo 2012; Kalirai, Marigo & Tremblay 2014). As a consequence, the growth of the core mass is smaller in models adopting CBM than in models not including it, or adopting a less efficient CBM. This aspect can be clarified looking at Fig. 3. The CBM profiles from the m3z2m2 model and **RI18** are shown. The dark shaded area represents the convective envelope, with the Schwarzschild boundary placed at the left border. Typically, the convective mixing coefficient in the envelope is around  $\text{Log}(D/(\text{cm}^2 \text{ s})) \sim 15$ . In

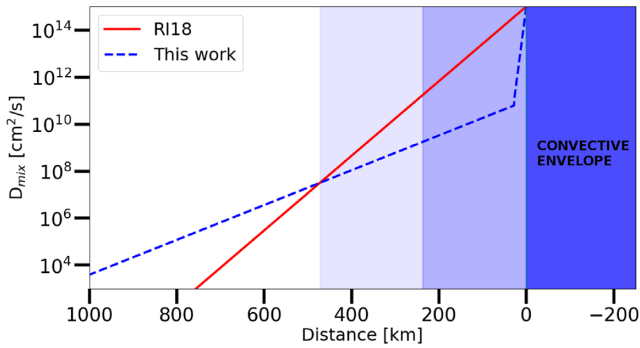


**Figure 3.** CBM profiles from the m3z2m2 model and RI18 are shown. The dark shaded area represents the convective envelope, with the Schwarzschild convective boundary being the left border. RI18 mixing dominates over our prescription in the mid- and light shaded areas, with an efficiency higher than 100 times in the mid-shaded one.

**Table 2.** The CBM parameters adopted during TDU events are given (see the text for details) for the models shown in Table 1. The  $3 M_{\odot}$ ,  $Z = 0.02$  model from RI18 is shown as a comparison to model m3z2m2. We added two additional model with  $Z = 0.02$  and  $Z = 0.03$  to test the impact of more efficient TDUs.

Name	$f_1$	$D_2[\text{cm}^2 \text{s}^{-1}]$	$f_2$
m2z1m2	0.014	$10^{11}$	0.27
m3z1m2	0.014	$10^{11}$	0.27
m2z2m2	0.014	$10^{11}$	0.27
m3z2m2	0.014	$10^{11}$	0.27
RI18 ( $3 M_{\odot}$ , $Z = 0.02$ )	0.126	–	–
m2z3m2	0.014	$10^{11}$	0.27
m3z3m2	0.014	$10^{11}$	0.27
m3z2m2-hCBM	0.014	$4.3 \times 10^{11}$	0.27
m3z3m2-hCBM	0.014	$4.3 \times 10^{11}$	0.27

RI18 the mixing coefficient decays exponentially as a function of distance from the Schwarzschild boundary, using the exponential overshooting formalism of Herwig (2000). In order to consider the IGW contribution, which is not included in RI18, we adopt the double-exponential CBM of Battino et al. (2016). The CBM input parameters for all models in Table 1 are given in Table 2. All three input parameters were calibrated to fit the IGW-mixing profile by Denissenkov & Tout (2003) in the layers where the  $^{13}\text{C}$ -pocket forms, as shown in Fig. 4. Hence, no fine-tuning was done to directly match observables, since this calibration is purely theory and simulations based. In Table 2, we include the  $3 M_{\odot}$ ,  $Z = 0.02$  model from RI18 for comparison, which only required the  $f_1$  parameter since it was calculated with the single exponential overshooting scheme of Herwig (2000). We also add two models, m3z2m2-hCBM and m3z3m2-hCBM, calculated with a  $D_2$  parameter 4.3 times larger than the others, consistent with the typical IGW mixing uncertainty described by Denissenkov & Tout (2003). As a consequence, it experiences more efficient TDUs and form larger  $^{13}\text{C}$ -pockets.

In Fig. 3 we compare the CBM profiles from the m3z2m2 model and RI18. It is important to notice how the CBM profile in RI18 is more than two orders of magnitude higher in the medium-shaded area compared to the CBM adopted here, i.e. in the intershell zone immediately below the convective envelope. In this area the mixing coefficient in RI18 is still high enough to impact the TDU  $\lambda$  value, hence directly lowering the core mass. This picture is consistent with the  $\lambda$  temporal evolution shown in Fig. 5. A

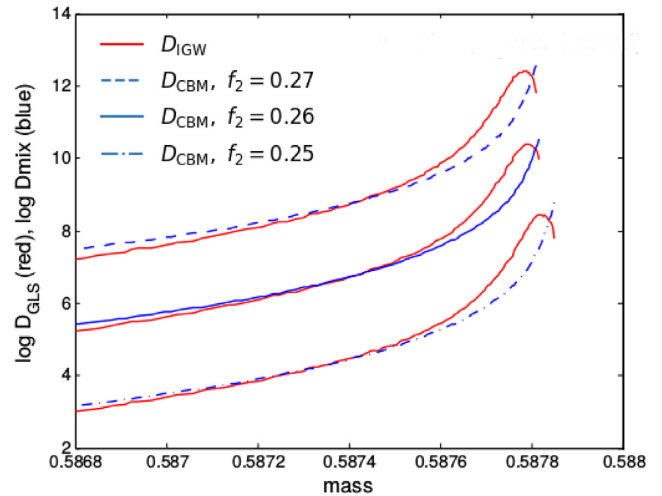


**Figure 4.** Comparison between the diffusion coefficient profile calculated using the GLS prescription for the IGW mixing from Denissenkov & Tout (2003) (the red curves) and the one derived for the CBM with the parametrization used in this work (the blue curves). The dot-dashed, solid, and dashed blue curves with their adjacent red curves show comparisons for the cases of  $f_2 = 0.25$ ,  $f_2 = 0.26$ , and  $f_2 = 0.27$ . To make them more visible, the dashed and dot-dashed lines are shifted along the vertical axis by  $\log(D) = 2$  up and down relative to the solid line. The bump on the  $\log(D_{\text{GLS}})$  profile near the convective boundary is due to a rapid decrease of the thermal diffusivity  $K$  with depth accompanied by a fast increase of the buoyancy, and by the fact that  $D_{\text{GLS}}$  is proportional to  $NK$  (equation 15 in Denissenkov & Tout 2003). The  $f_2 = 0.27$  case has been selected as standard since it provides the best fit of the IGW profile in the layers where the  $^{13}\text{C}$ -pocket forms ( $7 < \text{Log}(D_{\text{mix}}) < 8$ ).

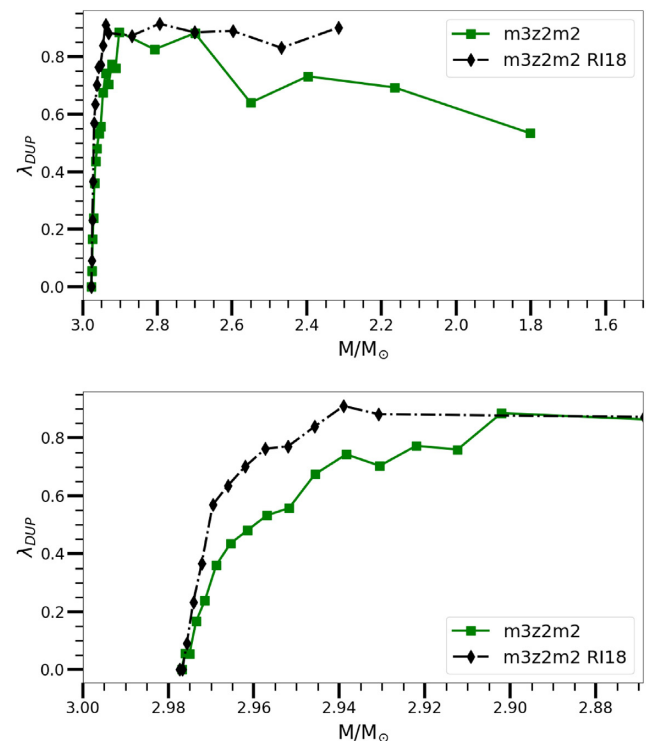


**Figure 5.** TDUs efficiency ( $\lambda$ ) temporal evolution. A comparison between m3z2m2 and RI18 is shown in the upper panel, while a zoom into the early AGB-phase is shown in the lower panel.

**Table 3.** Total number of TPs and number of TPs occurring during the AGB oxygen-rich phase for the same models shown in Table 2. The  $3 M_{\odot}$ ,  $Z = 0.02$  model from **RI18** is shown as a comparison to models m3z2m2 and m3z2m2-hCBM.

Name	Total TPs	O-rich TPs
m2z1m2	25	18
m3z1m2	16	8
m2z2m2	30	27
m3z2m2	24	15
m3z2m2-hCBM	23	15
<b>RI18</b> ( $3 M_{\odot}$ , $Z = 0.02$ )	21	13
m2z3m2	30	29
m3z3m2	31	20
m3z3m2-hCBM	30	19

dedicated comparison between m3z2m2 and **RI18** is shown in the upper panel, while a zoom into the early AGB-phase is shown in the lower panel. The plot shows how TDUs in the **RI18** model have a systematically higher  $\lambda$  (starting already in the early stage of the AGB) because of the higher CBM efficiency in the stellar layers right below the convective envelope. This indeed impacts as well the core mass in an indirect way: every TDU causes a surface enrichment in primary carbon, causing the surface C/O ratio to increase. As soon as the number of carbon atoms exceeds that of oxygen (passing from the oxygen-rich phase to the carbon-rich phase, i.e.  $C/O > 1$ ) a sudden rise in the atmospheric opacity occurs (Marigo 2002). This results in an envelope expansion, lower effective temperatures, and increased mass-loss from dust-driven winds (Marigo & Girardi 2007; Mattsson, Wahlin & Höfner 2010; Nanni et al. 2018). Therefore, the AGB lifetime is shorter and consequently also the number of TPs and TDUs experienced by the star, making the growth of the core mass smaller than otherwise predicted in models with a slower carbon surface enrichment due to less efficient TDUs (Kalirai et al. 2014). Table 3 shows the total number of TPs and number of TPs occurring during the oxygen-rich AGB phase. Also the  $3 M_{\odot}$ ,  $Z = 0.02$  model from **RI18** is shown as a comparison with m3z2m2, showing a significant reduction of the total number of TPs. This is visible already during the oxygen-rich phase, during which **RI18** model needs two TPs less to become carbon rich. The same conclusions can be reached looking at the Kippenhahn diagrams in Fig. 6, where our m3z2m2 is again compared to **RI18**: location of convective boundaries and core mass as a function of time are presented. In particular, the formation of the PDCZ is visible every time a TP occurs.  $\lambda$  temporal evolution for all the other models listed in Tables 1 and 3 is shown in Fig. 7.

### 3.2 $^{13}\text{C}$ -pocket formation and intershell abundances

As mentioned in Section 1 and as described in Battino et al. (2016), the most direct impact of our CBM model is an increased  $^{13}\text{C}$ -pocket size [defined as the mass-coordinate difference between the points where the mass fraction of  $^{13}\text{C}$ ,  $X(^{13}\text{C})$ , exceeds 0.001 and  $X(^{13}\text{C}) > X(^{14}\text{N})$ ] compared to **RI18**, where the classic single exponentially decaying diffusion mixing scheme is adopted. Fig. 8 compares two  $^{13}\text{C}$ -pockets, from our m2z1m2 model and the corresponding model in **RI18**, around the same mass coordinate and at the beginning of the carbon-rich phase. It shows how the pocket size is larger by around a factor of three. This is due to the less steep hydrogen profile formed by our CBM model compared to **RI18**, when the convective envelope reaches the maximum penetration into the He-intershell during TDUs. In this way, hydrogen mass fraction

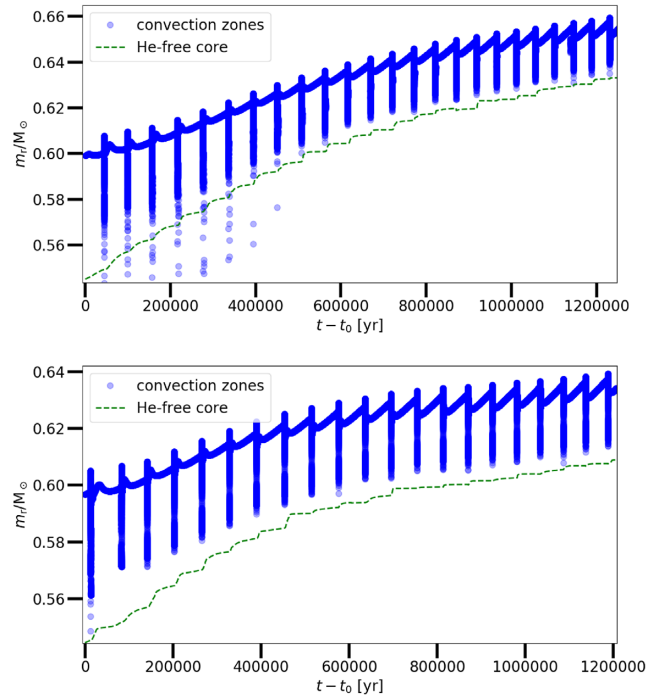


**Figure 6.** Upper panel: Kippenhahn diagram of m3z2m2. The whole AGB phase is presented zoomed in the He-intershell. Lower panel: same as in the upper panels, but for **RI18**.

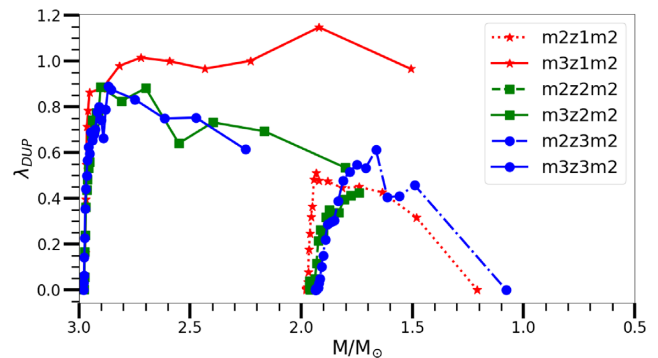


**Figure 7.** TDU efficiency  $\lambda$  temporal evolution as a function of total mass for all the models listed in Table 1.

decreases more slowly moving towards the centre of the star. This allows  $X(^{13}\text{C})$  to exceed 0.001 in a larger portion of the intershell, and hence a larger  $^{13}\text{C}$ -pocket. As we will see in the following sections, this is causing a higher production of  $s$ -process elements. In addition to the pocket size, another important feature, from the comparison between our models and **RI18**, is the very similar abundance peak value of  $^{13}\text{C}$  inside the pocket. This is directly linked to the almost identical  $^{12}\text{C}$  abundance in the intershell during the interpulse period, which comes from the same CBM adopted at the intershell bottom during TDUs. Moreover, including CBM during TDUs at the intershell bottom is very important to reproduce key observables like surface abundances of H-deficient post-AGB stars (Werner & Herwig 2006; Battino et al. 2016), as this is to date the only way to reproduce the observed enrichment in carbon and oxygen, at the expenses of helium abundance, in the intershell at the end of the AGB phase. This is shown in Fig. 9, where final intershell abundances of m2z1m2 are compared to surface abundance of four

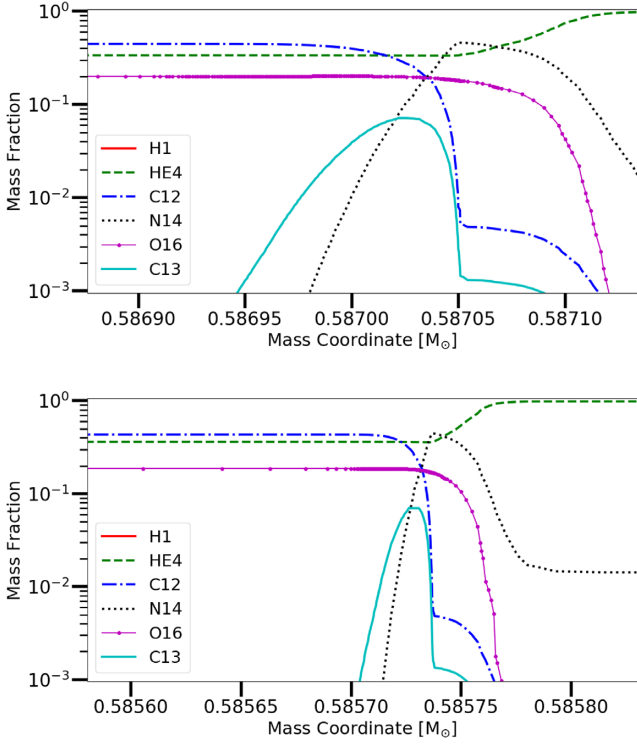


**Figure 8.** Upper panel:  $^{13}\text{C}$ -pocket at the beginning of the carbon-rich phase from m2z1m2. Lower panel:  $^{13}\text{C}$ -pocket at the beginning of the carbon-rich phase from RI18 at the same mass coordinate as in the upper panel. The comparison shows a much larger pocket compared to RI18.

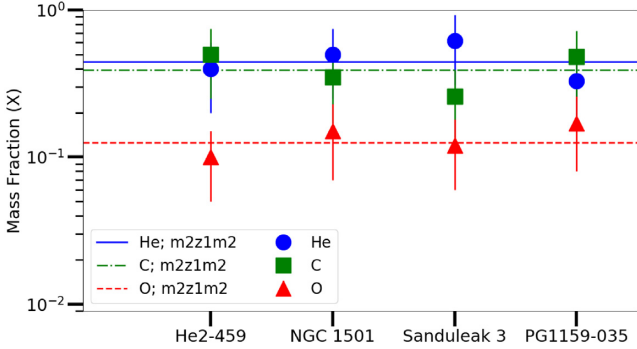


**Figure 9.** Final intershell abundances of m2z1m2, which are representatives for all the other models, are compared to surface abundance of four representatives H-deficient post-AGB stars.

representatives H-deficient post-AGB stars, showing a very good agreement between our model with observations. High abundances of  $^{12}\text{C}$  in the He-intershell region cause high  $^{13}\text{C}$  abundances and a more efficient neutron flux in the  $^{13}\text{C}$ -pocket. At the same time, lower abundances of  $^4\text{He}$  lead to higher temperatures during the TP, leading to a stronger activation of the  $^{22}\text{Ne}$  neutron source (Lugaro et al. 2003b, 2018).

### 3.3 Approximating rotationally induced mixing: models with additional constant mixing coefficient

Busso et al. (2001) presented a compilation of *s*-process observational data, including the ratio of the *s*-process production around the barium peak (hs) over the nucleosynthesis around the strontium

peak (ls). In particular,  $-0.6 < [\text{hs}/\text{ls}] < 0.0$  characterizes stars of solar metallicity, adopting the square-bracket notation defined as:

$$[X/Y] = \log((X_*/Y_*)/(X_\odot/Y_\odot)) \quad (2)$$

with  $X_*/Y_*$  and  $X_\odot/Y_\odot$  being the ratios of two quantities measured in a given star and in the Sun, respectively. It also seems that models applying CBM at the bottom of the He-intershell during TPs can reproduce only the largest observed hs/ls ratios, suggesting a neutron exposure in the  $^{13}\text{C}$ -pocket at the maximum of the observed range (Lugaro et al. 2003b; Herwig 2005). The first study where the IGW-driven CBM was tested and calibrated was done by Battino et al. (2016): the stellar models presented were all non-rotating and  $[\text{hs}/\text{ls}]$  0.0 was obtained. On the other hand, Herwig et al. (2003), Siess, Goriely & Langer (2004), and Piersanti, Cristallo & Straniero (2013) have shown that by considering rotation in AGB models the final  $[\text{hs}/\text{ls}]$  ratio tends to be reduced compared to non-rotating models. The reason for this is that during the AGB phase the slowly rotating envelope and the fast-rotating compact core are in contact. Hence, shear mixing sets in during the interpulse period polluting the  $^{13}\text{C}$ -pocket with the neutron poison  $^{14}\text{N}$  from the  $^{14}\text{N}$ -pocket just above (also visible in Fig. 8), reducing the neutrons available for the *s*-process, in particular the neutron/seeds numeric ratio, hence the barium-peak production. The inclusion of a stochastic process like rotation, where a range of initial angular velocities is possible, could explain the spread in *s*-process efficiencies, observed in spectroscopic data and laboratory measurements of some isotopic ratios in pre-solar grains (Herwig et al. 2003; Herwig 2005; Battino et al. 2016). We are not going to present models including a self-consistent implementation of rotation, yet, given the essential role rotation-induced mixing has in reproducing AGB observables, we want to explore its possible impact in *s*-process nucleosynthesis. For this reason, we apply a low constant mixing across the intershell during the interpulse period, in order to mimic the effects of shear mixing, following a method very similar to Herwig et al. (2003); models with rotationally induced mixing predict mixing coefficients around  $\log(D[\text{cm}^2 \text{s}^{-1}]) \sim 2$ , which eventually totally suppress the *s*-process production by an excessively large poisoning of the  $^{13}\text{C}$ -pocket. Cantiello et al. (2014) showed that models only accounting for angular momentum conservation (as in Herwig et al. 2003) produce cores rotating about 10–1000 times faster than what has been found from asteroseismology, suggesting a missing angular momentum transport process. Since rotationally shear mixing coefficients depend on the square of the vertical velocity gradient (Zahn 1992; Maeder & Meynet 2000; Mathis, Palacios & Zahn 2004) and the compact core rotates with velocity  $v_{\text{core}}$ , faster than but similar in order of magnitude to the expanded envelope which rotates with velocity  $v_{\text{env}}$ , so that  $v_{\text{core}} \sim C \times v_{\text{env}}$  (typically  $2 \lesssim C \lesssim 4$ , see Deheuvels et al. 2015), we have:

$$D_{\text{rot}} \sim (K/N^2)(dv/dr)^2 \sim (K/N^2)((v_{\text{core}} - v_{\text{env}})/\delta(r))^2, \quad (3)$$

where  $K$  is the thermal diffusivity,  $N$  the Brunt-Väisälä frequency, and rotational velocity changes from  $v_{\text{core}}$  to  $v_{\text{env}}$  over a distance  $\delta(r)$  along the stellar radius. Therefore, if  $v_{\text{core}}$  from models is 10–1000 times faster than observed (as suggested by asteroseismology), then the expected mixing coefficients from rotationally induced mixing should decrease from  $\log(D_{\text{rot}}/(\text{cm}^2 \text{s}^{-1})) \sim 2$  to  $-4 < \log(D_{\text{rot}}/(\text{cm}^2 \text{s}^{-1})) < 0$ . Hence, in order to mimic the effects of shear mixing and following a method very similar to what was done in Herwig et al. (2003), we present in Table 4 six additional models with an additional low constant mixing across the intershell,

**Table 4.** List of AGB models with additional internal constant mixing to mimic the effects of rotation: initial mass, initial metallicity, initial and final H-free core mass, total lifetime, and logarithmic value of constant mixing coefficient are given. For comparison, also m3z2m2 and m3z3m2 models already introduced in Table 1 are presented.

Name	$M_{\text{ini}} [M_{\odot}]$	$Z_{\text{ini}}$	H-Free $M_{\text{ini}} [M_{\odot}]$	H-Free $M_{\text{end}} [M_{\odot}]$	$\tau_{\text{tot}} [\text{yr}]$	Total TPs	TPs O-rich	$\text{Log}_{10}(D_{\text{mix}})$
m3z2m2	3	0.02	0.599	0.659	$4.85 \times 10^8$	24	15	–
m3z2m2-rotmix.stx2	3	0.02	0.599	0.657	$4.83 \times 10^8$	24	17	–0.4
m3z2m2-rotmix.st	3	0.02	0.599	0.659	$4.83 \times 10^8$	25	16	–0.7
m3z2m2-rotmix.std2	3	0.02	0.599	0.656	$4.83 \times 10^8$	25	16	–1
m3z3m2	3	0.03	0.562	0.650	$6.03 \times 10^8$	31	20	–
m3z3m2-rotmix.st	3	0.03	0.562	0.645	$6.05 \times 10^8$	30	21	–0.7
m3z3m2-hCBM-rotmix.stx1p5	3	0.03	0.562	0.639	$6.05 \times 10^8$	30	19	–0.5
m3z3m2-hCBM-rotmix.st	3	0.03	0.562	0.640	$6.05 \times 10^8$	31	20	–0.7

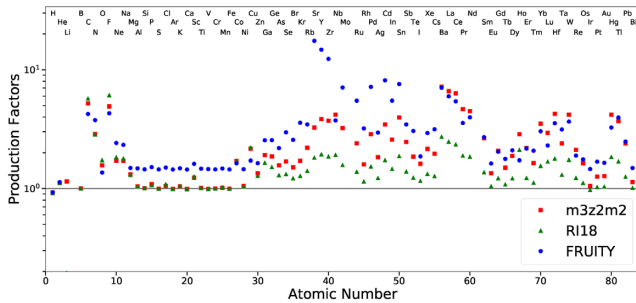


**Figure 10.** Comparison of heavy elements production factors between m3z2m2, RI18, and FRUITY models.

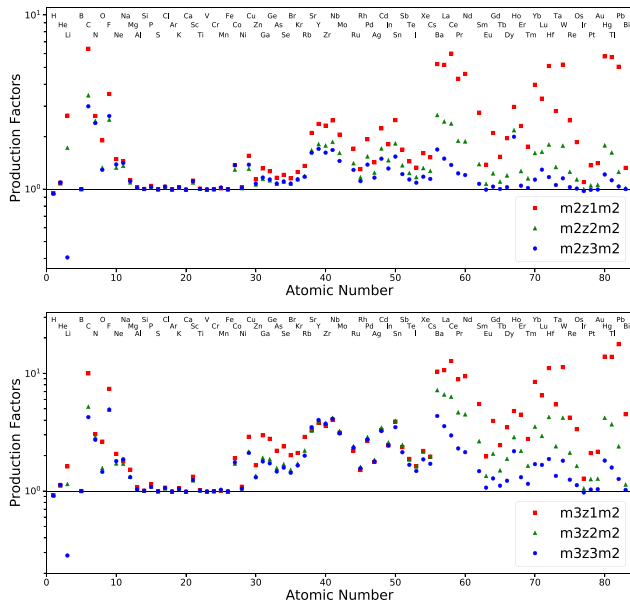


**Figure 11.** Upper panel: Heavy elements production factors of  $2 M_{\odot}$  models listed in Table 1. Lower panel: Same as in the upper panel, but for  $3 M_{\odot}$  models.

consistent in the range we have just defined, during the interpulse period. It is anyway important to notice the big assumption we are making here, that is stellar rotation being an efficient extra-mixing source in AGB stars. This is actually still a matter of debate (see Herwig 2005; Deheuvels et al. 2015; Straniero, Cristallo & Piersanti 2015). On the other hand, any extra-mixing process able to satisfy the conditions described above could be considered.

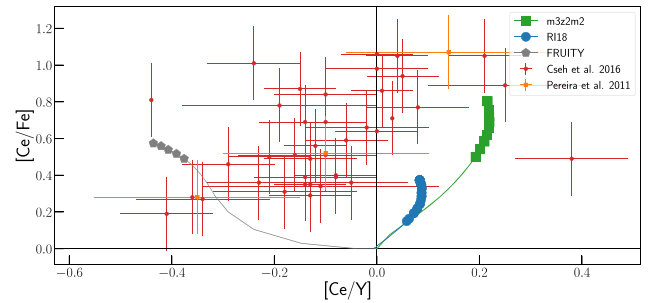


**Figure 12.** Comparison of  $[\text{Ce}/\text{Fe}]$  versus  $[\text{Ce}/\text{Y}]$  index from m3z2m2 with same mass and metallicity models from RI18 and the FRUITY data base. Also observational data of barium stars from Cseh et al. (2018) and Pereira et al. (2011) are shown. Considering observational uncertainties, only stars with a  $[\text{Fe}/\text{H}]$  consistent with the stellar models shown are included (i.e.  $-0.05 < [\text{Fe}/\text{H}] < 0.15$ ).

#### 4 POST-PROCESSING NUCLEOSYNTHESIS CALCULATIONS

The  $s$ -process nucleosynthesis in low-mass AGB stars heavily depends on the properties of the  $^{13}\text{C}$ -pocket. As already described, the stellar models presented in this work form a  $^{13}\text{C}$ -pocket that is about three times larger than in RI18. This has profound consequences on the resulting heavy element production, as shown in Fig. 10. Models described in RI18 exhibit a low  $s$ -process production compared to what is inferred from spectroscopic observations. Changing the treatment of convective boundaries according to Battino et al. (2016), results in about three times larger  $s$ -process production factors in agreement with observations. In the same figure, we also show the results from FRUITY calculations (Cristallo et al. 2011). The gap in barium production when comparing RI18 and FRUITY is not present anymore in this work, while the difference persists when considering Sr peak abundances. This is due to FRUITY models not including any CBM at the base of the PDCZ. This leads to lower  $^{12}\text{C}$  abundances in the intershell in FRUITY models, hence lower  $^{13}\text{C}$  abundances and a less efficient neutron flux in the  $^{13}\text{C}$ -pocket, which favours Sr-peak over Ba-peak elements (see Lugaro et al. 2003a). The production factors of all our models are shown in Fig. 11: in particular, lower metallicity models show a stronger production of the second (Ba region) and third (Pb region)  $s$ -process peaks, while the first peak (strontium region) is favoured in higher metallicity models. In Fig. 12 we show the tracks of m3z2m2 and the models with the same initial mass and metallicity in RI18 and FRUITY. Since there are now large enough and internally consistent data sets of individual elements representing second-peak (hs) and first-peak (ls) elements, each symbol in the figure gives the surface  $[\text{Ce}/\text{Y}]$  and

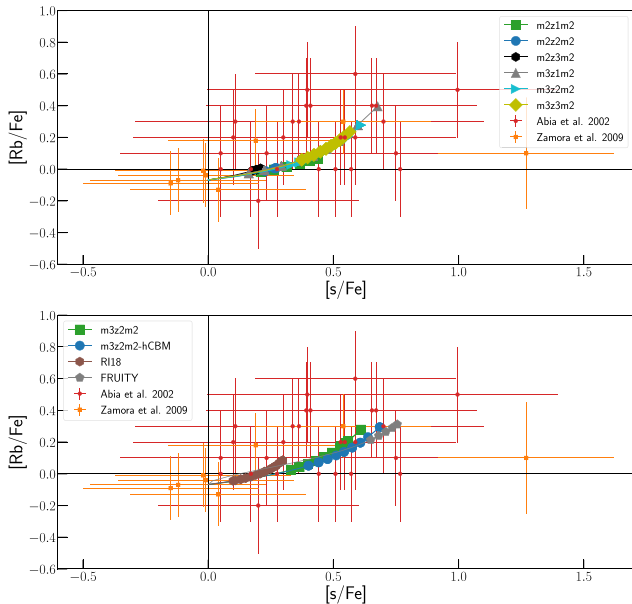


**Figure 13.** Upper panel: Comparison of Rb abundance versus the total  $s$ -process production inferred from spectroscopy analysis of carbon stars by Abia et al. (2002) and Zamora et al. (2009) with the abundance predicted by our models in Table 1. Lower panel: Same as in the upper panel, but comparing m3z2m2 with same mass and metallicity models from RI18 and the FRUITY data base. We also show predictions from m3z2m2-hCBM, whose comparison with m3z2m2 shows the impact of the increased  $^{13}\text{C}$ -pocket size due to higher CBM efficiency during TDUs.

[Ce/Fe], being an update to the classic [hs/lS] and [hs/Fe] indices, respectively, as discussed by Cseh et al. (2018). The theoretical tracks are compared to the largest homogeneous set of Ba giant star observations presented in Cseh et al. (2018), including data from Pereira et al. (2011) to achieve a better statistic at supersolar metallicities. As the star evolves, TDU events gradually enrich the envelope in carbon eventually resulting in surface  $\text{C/O} > 1$ , entering the carbon-rich phase that we indicate with bigger size symbols. The figure shows the larger  $s$ -process efficiency in the m3z2m2 and FRUITY model compared to RI18, demonstrated by the higher [Ce/Fe] value. Additionally, since the intershell material in RI18 and m3z2m2 has the same [Ce/Y] the two tracks initially perfectly overlap, while FRUITY model evolves towards negative [Ce/Y] values, reflecting the absence of CBM under the PDCZ as previously discussed. This is not surprising, since both RI18 and m3z2m2 models treat the CBM at the bottom of the intershell during TP in the same way, resulting in very similar  $^{12}\text{C}$  intershell abundance (as seen in Section 3.2) and hence neutron exposures. Because of the larger amount of  $s$ -process material brought to the surface at every TDU, the m3z2m2 track is pushed further away from the origin towards a higher final [Ce/Y].

#### 4.1 Comparison with spectroscopic observations

Low-mass AGB stars produce the bulk of the  $s$ -process material in the  $^{13}\text{C}$ -pocket, but a non-negligible amount of neutrons comes from  $^{22}\text{Ne}(\alpha, n)^{25}\text{Mg}$  activated during the TP. Additionally, some isotopes in proximity of branching points are efficiently produced only in the high neutron density conditions achieved during the TP (Raut et al. 2013). One example is rubidium, whose neutron magic isotope  $^{87}\text{Rb}$  is produced only in high enough neutron

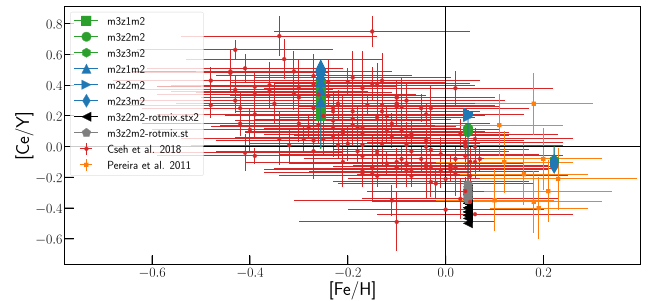


**Figure 14.** Comparison of [Ce/Y] versus [Fe/H] results from the whole evolution of models listed in Table 1 adding also m3z3m2.rotmix.st and m3z2m2.rotmix.stx2, which include an artificial mixing to replicate stellar rotation effects. The values inferred from spectroscopy analysis of barium stars by Cseh et al. (2018) and Pereira et al. (2011) are also shown as comparison.

density conditions to open the branching at  $^{86}\text{Rb}$  (18.642 d half-life). Spectroscopic observables allow access to Rb abundances as well as abundances of other  $s$ -process elements produced entirely in the  $^{13}\text{C}$ -pocket. Fig. 13 shows the rubidium abundance versus the total  $s$ -process production inferred from spectroscopy analysis of carbon stars compared to the predictions by our models. The  $s$ -process production is described by the [s/Fe] index, expressed with formalism defined by equation (2), with the numerator being the averaged abundance between Sr and Ba peak elements. The slope of our models' tracks is in agreement with the observed relative contribution of the TP with respect to the  $^{13}\text{C}$ -pocket. Moreover, we are able to reproduce the highest observed  $s$ -process production within observational uncertainties. As described in Busso et al. (2001), a range of  $^{13}\text{C}$ -pocket sizes is required to reproduce the spread of [hs/lS], and hence [Ce/Y], observed in stars for a given metallicity. Indeed, a stochastic process like rotation could produce this effect, as described in Section 3.2 (see also Herwig et al. 2003; Herwig 2005). Indeed, the higher the initial rotational velocity, the lower the final [Ce/Y]. As a consequence, stellar models not including rotation should reproduce the highest observed [Ce/Y] values observed (Herwig 2005). This is successfully reproduced by our models, as shown in Fig. 14. We plot the results from the whole evolution of the models listed in Table 1, adding also two of the models described in Table 4, which include an artificial mixing to replicate stellar rotation effects. The theoretical predictions reproduce the [Ce/Y] versus [Fe/H] slope around solar metallicity, as well as the observed spread in [Ce/Y] for specific metallicities. Moreover, we present another similar comparison in Fig. 15, where we show our final surface abundances and include the results from FRUITY and Monash group (Karakas & Lugaro 2016) data sets. Similar to what previously discussed about FRUITY results, Monash models do not include any CBM at the base of the PDCZ, hence a lower final [Ce/Y] compared to our models. Additionally, our models including rotational mixing present a final [Ce/Y] on average 0.4 dex lower than our standard setting, suggesting rotational mixing as a strong candidate to cover the whole observed range of  $s$ -process efficiencies. However, it is important to notice the possibility that the necessary stochasticity to reproduce the observed spread in [Ce/Y] may be present in CBM processes already. Our understanding of convection, which is the physical process originating IGW and hence CBM in our models, is not in a satisfying state yet. The picture gets even more complicated when considering additional

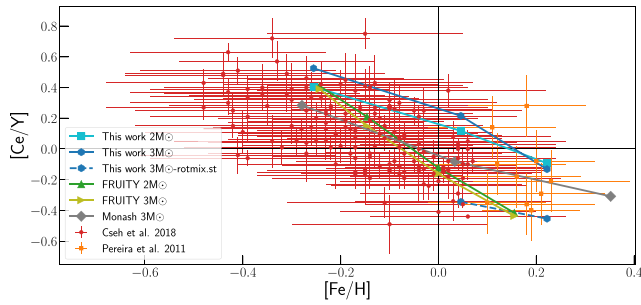


**Figure 15.** Comparison of [Ce/Y] versus [Fe/H] results from the final surface abundances of models presented in Fig. 14 here we also include results from the FRUITY data base and Monash models as a comparison.

physics like magnetic fields that have already been proposed to play a key role in the formation of the  $^{13}\text{C}$ -pocket (see Trippella et al. 2016), whose interplay with IGW has not been investigated yet. This may introduce a stochastic component in the CBM process, resulting in the spread of neutron exposures and  $^{13}\text{C}$ -pocket sizes, possibly including the results obtained by R118.

## 4.2 Comparison with pre-solar grains measurements

When the condition  $\text{C/O} > 1$  is met and a carbon star is formed, a sudden rise of the opacity occurs, making the atmosphere expand and cool (Marigo 2002; Kalirai et al. 2014). In these conditions silicon carbide (SiC) grains can form. The vast majority of SiC grains (‘mainstream’ SiC, more than 90 per cent of SiC grains) form in the atmospheres around carbon-rich AGB stars (Ferrarotti & Gail 2006; Nanni et al. 2013; Lugaro et al. 2018). Each specific grain formed in a single specific stellar source.

Recently, Lugaro et al. (2018) compared predictions from AGB models computed with the Monash stellar structure code (Karakas & Lattanzio 2007) with isotopic ratio measurements, focusing on Zr, Sr, and Ba isotopic ratios, matching measurements from Liu et al. (2014) and Liu et al. (2015). On the other hand, a number of limitations in the stellar models were also highlighted, the most important of these being the absence of any CBM at the base of the TP-driven convective zone, despite the indications from multi-D hydrodynamic simulations (Herwig et al. 2007) and observations of H-deficient post-AGB stars as described in Section 3.2. In the same section, we explained how the enhancement in  $^{12}\text{C}$ , following the mixing at the bottom intershell convective boundary results in a more efficient neutron flux in the  $^{13}\text{C}$ -pocket, hence favouring a higher production of Ba and La compared to models with no CBM at the bottom of the He-intershell. We also confirmed the stronger activation of the  $^{22}\text{Ne}$  neutron source, leaving a clear fingerprint in branching-point sensitive isotopic ratios like  $^{96}\text{Zr}/^{94}\text{Zr}$  (see Herwig 2005; Battino et al. 2016). It is then interesting to compare stellar models where such CBM processes are included, like in this work, to the stardust SiC data.

### 4.2.1 Sr

In Fig. 16 we compare our models with measured Sr isotopic ratios. Plotted values are given in  $\delta$ -value notation to represent the isotopic ratios, i.e. the permil variation with respect to the solar ratio (for which  $\delta = 0$ ), so that  $\delta = ((\text{model ratio}/\text{solar ratio}) - 1) \times 1000$ . Each symbol marking theoretical predictions corresponds to an interpulse period, with bigger size symbols corresponding to the

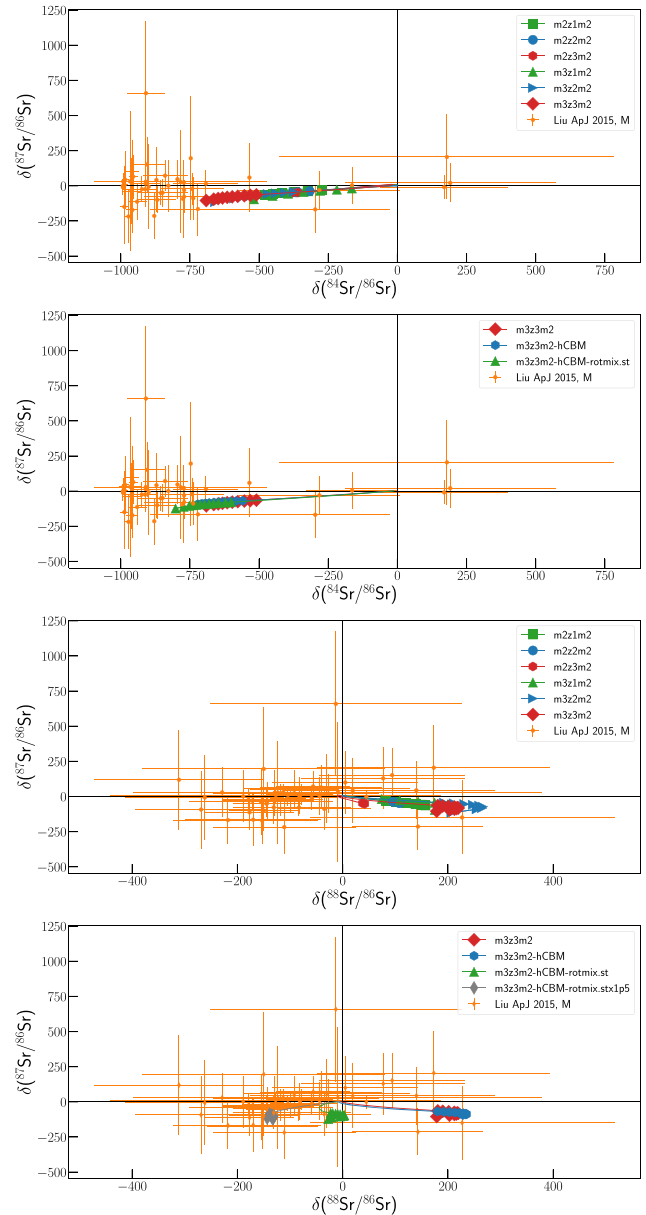


**Figure 16.** Comparison of stellar models presented in this work with measured Sr isotopic ratios from pre-solar SiC grains. Each symbol marking a theoretical prediction corresponds to an interpulse period, bigger size symbols corresponding to the carbon-rich phase. It is visible how rotation-induced mixing may help self-consistently cover the whole observed range, in particular in  $^{88}\text{Sr}/^{86}\text{Sr}$ . Error bars account for a  $2\sigma$  uncertainty.

carbon-rich phase, which is a necessary condition for grains to form. As visible in second and fourth panels, we tested both a larger TDU efficiency and rotation-induced mixing to consistently cover the whole observed range, with the latter having the largest impact. This is particularly important for  $^{88}\text{Sr}/^{86}\text{Sr}$ , where the neutron-magic  $^{88}\text{Sr}$  is depleted more and more by higher diffusion of  $^{14}\text{N}$  inside the  $^{13}\text{C}$ -pocket, as it would occur in faster rotating models. More precisely, Fig. 16 shows how a range of initial rotation velocity values, able to produce the additional intershell mixing between zero and the value inserted in m3z2m2-rotmix.stx1p5, would be able to cover the bulk of the observed values. Rotation also improves the comparison to measured  $^{84}\text{Sr}/^{86}\text{Sr}$  ratios, pushing the tracks towards the bulk of

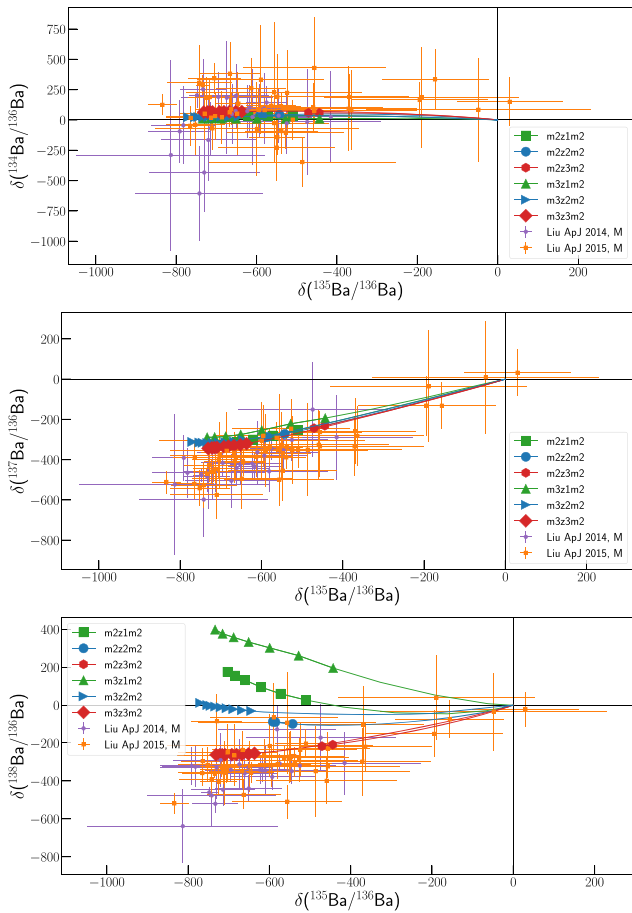


**Figure 17.** Comparison of stellar models presented in this work with measured Ba isotopic ratios from pre-solar SiC grains.

data which have typically values lower than 800, due to a lower destruction of  $^{86}\text{Sr}$  as a consequence of the lower neutron exposure, while  $^{84}\text{Sr}$  is unaffected being a  $p$ -only isotope. On the other hand, this is still not enough to reproduce the typical  $^{84}\text{Sr}/^{86}\text{Sr}$  measured from most of the grains, possibly suggesting a too weak depletion of  $^{84}\text{Sr}$ .

#### 4.2.2 Ba

In Fig. 17 we compare our models with measured Ba isotopic ratios.  $^{138}\text{Ba}/^{136}\text{Ba}$  from  $Z = 0.03$  models are consistent with observations. Hence,  $Z = 0.03$  models well compare with grains, as Lugaro et al. (2018) indicated. However, models with lower metallicity do not.

On the other hand, as shown in Fig. 18, the artificial inclusion of rotation-induced mixing pushes all our stellar tracks, including  $Z = 0.02$  models, down to lower  $\delta(^{138}\text{Ba}/^{136}\text{Ba})$ , as the neutron-magic  $^{138}\text{Ba}$  decreases with decreasing neutron exposure, closer to the experimental data from Liu et al. (2014) and Liu et al. (2015). In the same figure,  $m3z3m2$ -hCBM  $m3z3m2$  are also presented, showing how models with a larger  $^{13}\text{C}$ -pocket perform better in reproducing laboratory measurements. Additionally, we tested the lower limit of our adopted  $^{22}\text{Ne}(\alpha, n)^{25}\text{Mg}$  rate, the main neutron source at He-flash temperatures, by dividing it by a factor of two, consistently with a  $2\sigma$  variation according to the Monte Carlo calculation by Iliadis et al. (2010), whose recommended rate is very consistent with Jaeger et al. (2001). Interestingly, the stellar track is pushed

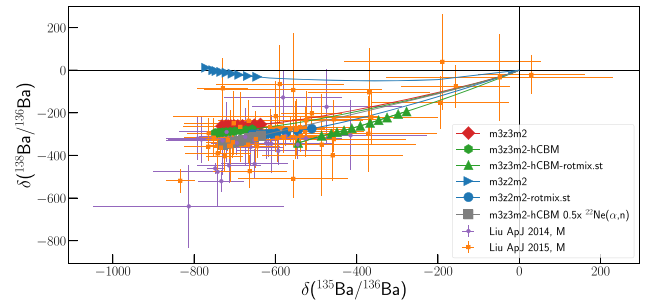


**Figure 18.** Comparison of  $\delta(^{138}\text{Ba}/^{136}\text{Ba})$  versus  $\delta(^{135}\text{Ba}/^{136}\text{Ba})$  from  $m2z2m2$ ,  $m2z3m2$ ,  $m3z2m2$ , and  $m3z3m2$ . We also included two models including artificial rotation-induced mixing,  $m3z2m2$ .rotmix.st and  $m3z2m2$ .rotmix.stx2.

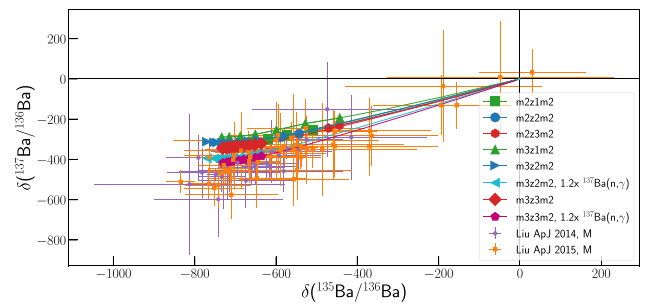


**Figure 19.** Comparison of  $m3z2m2$  and  $m3z3m2$   $\delta(^{137}\text{Ba}/^{136}\text{Ba})$  versus  $\delta(^{135}\text{Ba}/^{136}\text{Ba})$  with measurements from SiC grains: we show results obtained when adopting the  $^{137}\text{Ba}(n, \gamma)^{138}\text{Ba}$  given by Kadonis 0.3 (that we used as standard) to what is recommended in Kadonis 1.0 (i.e. a factor of 1.2 higher than Kadonis 0.3).

down right into the experimental data point, indicating how our models are actually in good agreement with laboratory data, within nuclear uncertainties.

Rotationally induced mixing does not impact  $\delta(^{134}\text{Ba}/^{136}\text{Ba})$  and  $\delta(^{137}\text{Ba}/^{136}\text{Ba})$ , since they mainly depend on the neutron-capture cross-sections: the models reproduce well the observed  $\delta(^{134}\text{Ba}/^{136}\text{Ba})$ , on the other hand it looks like it is not the case when comparing them with measured  $\delta(^{137}\text{Ba}/^{136}\text{Ba})$ . The  $^{137}\text{Ba}(n, \gamma)^{138}\text{Ba}$  reaction rate has been considerably increased (by a factor of 1.2) from Kadonis 0.3 (that we adopt) to Kadonis 1.0. Therefore, we tested this new rate in  $m3z2m2$  and  $m3z3m2$ . Indeed, Fig. 19 shows how pre-solar grains and our models prediction are in better agreement when using the newer  $^{137}\text{Ba}(n, \gamma)^{138}\text{Ba}$  rate.

Since Liu et al. (2015) provide Ba and Sr data coming from the same grain, we perform an additional comparison using the observed correlation between  $^{138}\text{Ba}/^{136}\text{Ba}$  and  $^{88}\text{Sr}/^{86}\text{Sr}$ . Fig. 20 shows that most of the grains present  $-200 < \delta(^{88}\text{Sr}/^{86}\text{Sr}) < 0$  and  $-400 < \delta(^{138}\text{Ba}/^{136}\text{Ba}) < -200$ . In the lower panel,  $m3z3m2$ -hCBM-rotmix.st,  $m3z3m2$ -hCBM-rotmix.stx1p5, and  $m3z2m2$ -rotmix.stx2 tracks successfully enter this specific area in the diagram, hence being able to explain the bulk of grains data. It is important to notice how all these three models are \*rotmix\* models, having all a slow constant extra-mixing active into the intershell, suggesting rotation-induced mixing as a strong candidate to explain the range of observed values in pre-solar grains. In particular,  $m3z3m2$ -hCBM-rotmix.st nicely reproduce the range of observed  $^{138}\text{Ba}/^{136}\text{Ba}$  values. At the same time, a range of stronger

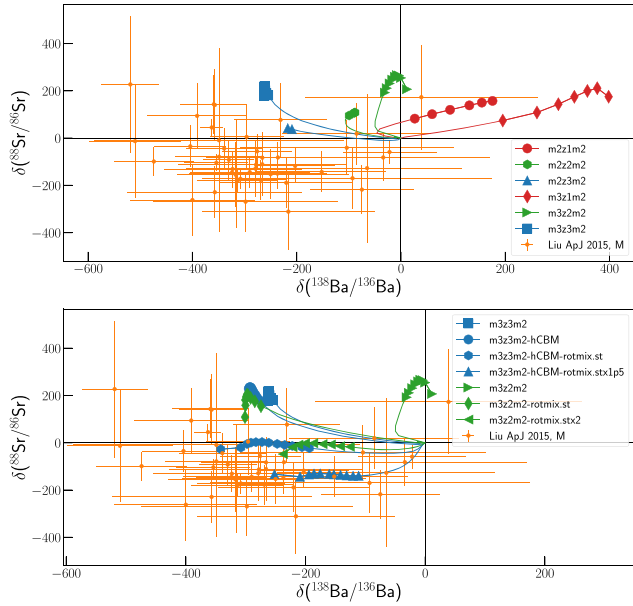


**Figure 20.** Correlated measurements of Sr and Ba of Liu et al. (2015), compared to our standard set in the upper panel and to models including artificial rotation-induced mixing in the lower one.

extra-mixing, as in m3z3m2-hCBM-rotmix.stx1p5, may effectively reproduce the observed  $^{88}\text{Sr}/^{86}\text{Sr}$  range.

#### 4.2.3 Zr

Fig. 21 shows the predictions of zirconium isotopic ratios for our models compared to Barzyk et al. (2007) measurements.  $^{90,91,92}\text{Zr}/^{94}\text{Zr}$  depend on the nucleosynthesis taking place in the  $^{13}\text{C}$ -pocket, while  $^{96}\text{Zr}/^{94}\text{Zr}$  also depends on TP conditions, since it is affected by the 64 d half-life branching point at  $^{95}\text{Zr}$  which can only be opened in high neutron density conditions. Models with higher metallicities produce lower  $^{96}\text{Zr}/^{94}\text{Zr}$  values for two reasons: (1) the higher the initial metallicity, the more first peak elements are favoured compared to second peak ones; (2) a higher metallicity affects stellar opacities and structure, resulting in lower TP temperatures and lower  $^{22}\text{Ne}(\alpha, n)^{25}\text{Mg}$  activation. Anyway, our standard settings apparently do not perform well when compared to observations, with the exception of the range of  $^{90}\text{Zr}/^{94}\text{Zr}$  values. In Fig. 22 we test m3z3m2 and m3z3m2-hCBM models with grains measurements, showing the model of RI18 as comparison: m3z3m2-hCBM performs better than m3z3m2, as it reproduces lower  $^{96}\text{Zr}/^{94}\text{Zr}$  achieving a better agreement with observations, even if still not good enough. The big difference between m3z3m2 and RI18 is mainly due to a different adopted  $^{95}\text{Zr}$  neutron-capture cross-section, that is in our case more than a factor of two lower than the rate used by RI18.  $^{13}\text{C}$ -pocket sizes in m3z3m2-hCBM are around  $10^{-4} M_{\odot}$  large in mass coordinate, a factor of about 1.5 larger than the typical pocket size in m3z3m2. This allows a higher  $^{94}\text{Zr}$  production and hence lower  $^{96}\text{Zr}/^{94}\text{Zr}$  after every TDU. The discrepancy with  $^{96}\text{Zr}/^{94}\text{Zr}$  could hence be reduced when larger  $^{13}\text{C}$ -pockets are considered. Indeed, our models were computed using the same CBM parametrization, calibrated on an  $M = 3 M_{\odot}$ ,  $Z = 0.02$  model (see Denissenkov & Tout 2003). A potential metallicity dependency of the CBM was then ignored at this stage. The impact of this approximation in the formation of the  $^{13}\text{C}$ -pocket will need to be studied in the future.

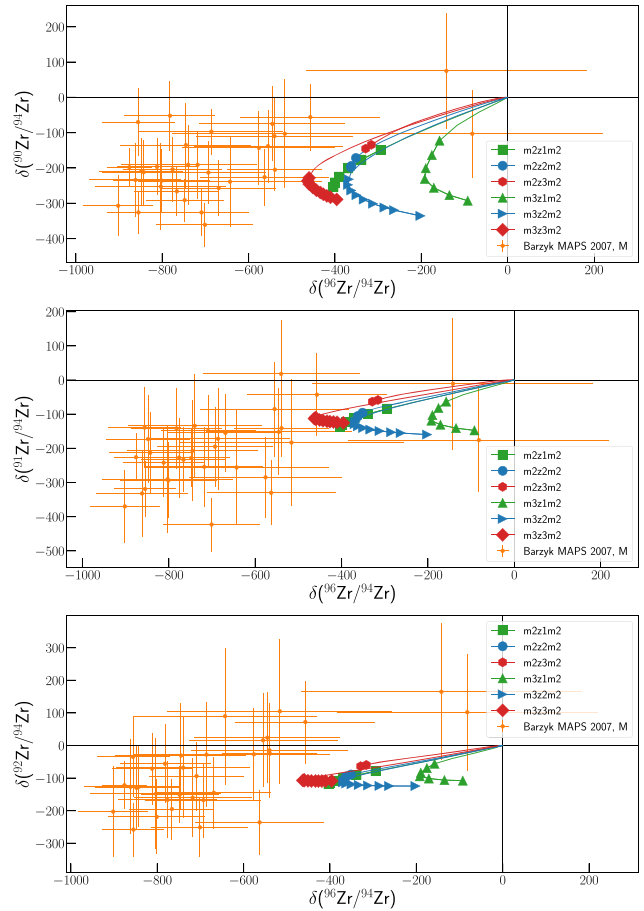


**Figure 21.** Comparison of stellar models presented in this work with Barzyk et al. (2007) measurements of Zr isotopic ratios.

In addition to the  $^{94}\text{Zr}(n, \gamma)^{95}\text{Zr}$ , Cescutti et al. (2018) also indicated  $^{95}\text{Zr}(n, \gamma)^{96}\text{Zr}$  as a key reaction rate for  $^{96}\text{Zr}$ . We therefore considered nuclear uncertainties with a potential impact on zirconium isotopes. In Fig. 23 we show the impact of the  $^{94}\text{Zr}(n, \gamma)^{95}\text{Zr}$  rate on our predictions. In particular, we apply a factor of 0.8 to the  $^{94}\text{Zr}(n, \gamma)^{95}\text{Zr}$  reaction rate to test the value recommended in Kadonis 0.3, since it is 20 per cent lower than the Lugaro et al. (2014) recommended rate that we adopted. In this case, the lowest measured values of  $^{91}\text{Zr}/^{94}\text{Zr}$  and  $^{92}\text{Zr}/^{94}\text{Zr}$  are now reproduced. Additionally, when the effects of rotation-induced mixing are included, also the highest values are explained. In summary, the effect of rotation-induced mixing, combined to neutron-capture reaction rate uncertainties, effectively reproduce the whole range of measured  $^{90}\text{Zr}/^{94}\text{Zr}$  (already reproduced by our standard set as shown in Fig. 21),  $^{91}\text{Zr}/^{94}\text{Zr}$ , and  $^{92}\text{Zr}/^{94}\text{Zr}$  values.

Fig. 24 shows that our prediction are in better agreement with laboratory measurements when considering stellar modelling and nuclear physics uncertainties: Lugaro et al. (2014) gives a factor of two uncertainty for  $^{95}\text{Zr}(n, \gamma)^{96}\text{Zr}$ , additionally we apply the same factor to test the lower limit of our adopted  $^{22}\text{Ne}(\alpha, n)^{25}\text{Mg}$ , in the same way as discussed in Section 4.2.2. The majority of grains data have  $-800 < \delta(^{96}\text{Zr}/^{94}\text{Zr}) < -600$  and m3z3m2-hCBM track successfully reproduce data in this interval, ranging between  $-750$  and  $-650$  in delta values during the carbon-rich phase. On the other hand it is not possible for our models to explain those grains

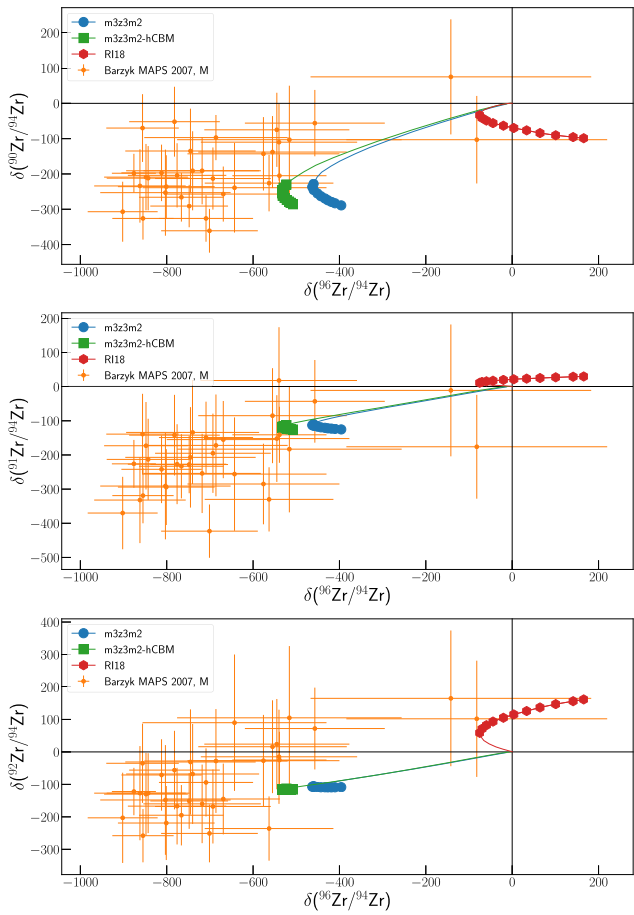


**Figure 22.** Same as in Fig. 21, but the results are shown for models m3z3m2 and m3z3m2-hCBM. The larger *s*-process production in m3z3m2-hCBM is a consequence of a <sup>13</sup>C-pocket 50 per cent larger in mass-coordinate compared to m3z3m2, leading to a stronger production of <sup>94</sup>Zr and hence decreasing the <sup>96</sup>Zr/<sup>94</sup>Zr isotopic ratio.

with  $\delta(^{96}\text{Zr}/^{94}\text{Zr}) < -800$ , failing to reproduce the whole  $^{96}\text{Zr}/^{94}\text{Zr}$  observed range.

#### 4.2.4 Mo

Figs 25 and 26 show predictions of isotopic ratios compared to Barzyk et al. (2007) measurements. The agreement is not satisfactory good for  $^{92}\text{Mo}/^{96}\text{Mo}$ ,  $^{95}\text{Mo}/^{96}\text{Mo}$ ,  $^{97}\text{Mo}/^{96}\text{Mo}$ , and  $^{100}\text{Mo}/^{96}\text{Mo}$ . In particular, in both figures  $^{92}\text{Mo}$  looks like it is not burned enough. Neutron captures on Mo isotopes are considerably different between Kadonis 0.3 and Kadonis 1.0, with  $^{96}\text{Mo}(n,\gamma)^{97}\text{Mo}$  also having an uncertainty around 20 per cent at <sup>13</sup>C-pocket temperatures. In Figs 25 and 26 we show predictions from m3z2m2 and m3z3m2 calculated with Kadonis 0.3 and m3z2m2 computed with Kadonis 1.0. We also show the predictions from m3z2m2 and m3z3m2-hCBM when Kadonis 0.3 is adopted, but with the  $^{96}\text{Mo}(n,\gamma)^{97}\text{Mo}$  from Kadonis 1.0 set to its lower limit (i.e. multiplied by a factor 0.8). We also show the results from the  $M = 3 M_{\odot}$ ,  $Z = 0.02$  model from RI18 as a comparison. First of all, it is evident how the comparison with pre-solar grains is definitely improved compared to RI18 due to the larger <sup>13</sup>C-pocket. The second aspect is that the observed  $^{97}\text{Mo}/^{96}\text{Mo}$  range can actually be explained within nuclear-physics uncertainties. Finally, considering

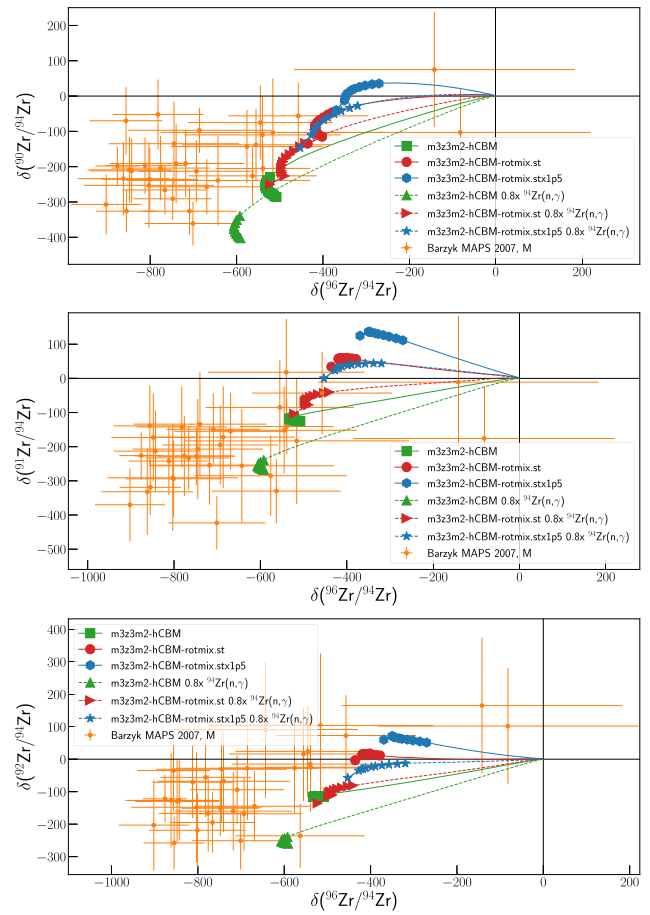


**Figure 23.** Same as in Fig. 21, but here we show the impact of the neutron-capture rate on <sup>94</sup>Zr on our theoretical predictions. In particular, we apply a factor of 0.8 to the  $^{94}\text{Zr}(n,\gamma)^{95}\text{Zr}$  reaction rate to test the value recommended in Kadonis 0.3, since it is 20 per cent lower than the Lugaro et al. (2014) recommended rate that we adopted. We also show the effect of rotation-induced mixing which, combined to neutron-capture reaction rate uncertainties, effectively reproduce the whole range of measured  $^{90}\text{Zr}/^{94}\text{Zr}$  (already reproduced by our standard set as shown in Fig. 21),  $^{91}\text{Zr}/^{94}\text{Zr}$ , and  $^{92}\text{Zr}/^{94}\text{Zr}$  values.

m3z2m2-hCBM, we notice how the bunch of grains with the lowest  $^{92}\text{Mo}/^{96}\text{Mo}$  observed could be reproduced with one more TDU event, which is well inside model uncertainties. On the other hand, even considering both nuclear and model uncertainties, our models are not able to reproduce the measured spread of  $^{95}\text{Mo}/^{96}\text{Mo}$  and  $^{100}\text{Mo}/^{96}\text{Mo}$ .

### 4.3 Key reaction rates

Table 5 shows the reaction rates we found important when comparing our results to observations. We identified six key reactions, five of them being neutron captures. Additionally, four out of five of these (n,γ) reactions have been classified as ‘Level 1’ key rates by Cescutti et al. (2018), which means they showed a strong correlation to the abundances of specific *s*-process isotopes listed in the second column. We hence agree with Cescutti et al. (2018) and propose them as candidates for improved measurement by future experiments, since more precise measurement of these rates will allow significantly more precise nucleosynthesis calculations. We also highlight the importance of  $^{95}\text{Zr}(n,\gamma)^{96}\text{Zr}$ , which is classified

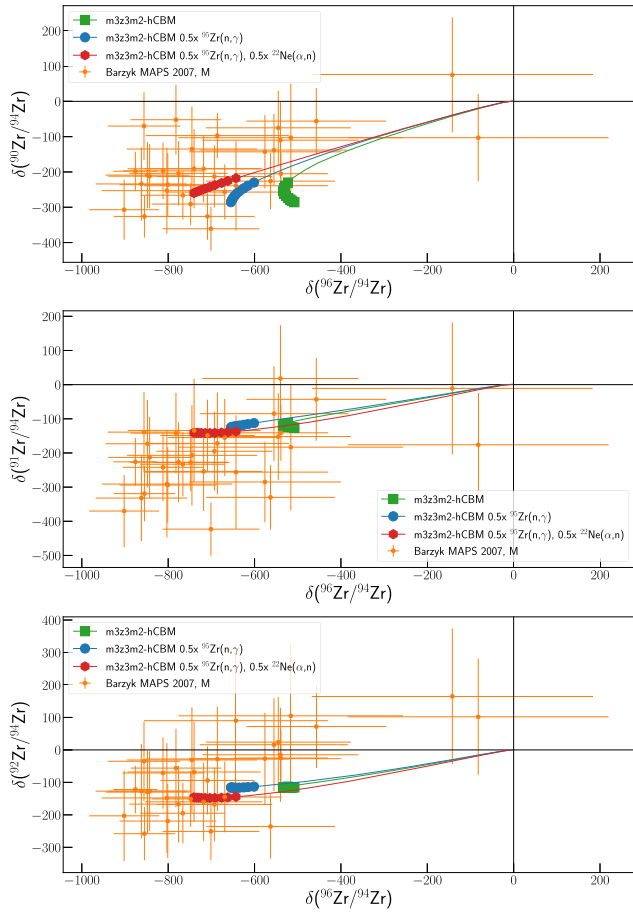


**Figure 24.** Same as in Fig. 21, but the results are shown for the models calculated varying key-reaction rates that impact the observed isotopic ratios (see the text for details).

as ‘Level 2’ key rate by Cescutti et al. (2018), hence less correlated to final abundances than ‘Level 1’ key rates. Despite this fact, we notice that this rate is actually the main source of the still significant uncertainty affecting  $^{96}\text{Zr}$ . Finally, we include in the list also the main neutron source during TP events, the  $^{22}\text{Ne}(\alpha,n)^{25}\text{Mg}$ , affecting branching-point sensitive isotopes like  $^{87}\text{Rb}$  and  $^{96}\text{Zr}$ .

#### 4.4 Ejected yields

We have calculated full yields for all our models. These are available in tables online at the CADC (The Canadian Astronomical Data Center, <http://www.cadc-ccda.hia-ihp.nrc-cnrc.gc.ca>) and can be analysed interactively through the web interface WENDI at [wendi.nugridstars.org](http://wendi.nugridstars.org). Table 6 shows a comparison between the yields presented in this work for  $m3z2m2$  and the yields presented by Karakas (2010) and Cristallo et al. (2011) for their models with same initial mass and metallicity. The final ejected masses of  $^{12}\text{C}$ ,  $^{14}\text{N}$ , and  $^{16}\text{O}$  for  $m3z2m2$  are 0.0340, 0.0070, and 0.0316  $M_{\odot}$ , respectively. For the same isotopes and the same star, RI18 provide 0.0445, 0.0077, and 0.0383, Karakas (2010) 0.0207, 0.0056, and 0.0211, and Cristallo et al. (2011) 0.0186, 0.0066, and 0.0211. For  $^{12}\text{C}$  we obtain an abundance that is factor of 1.83 and 1.64 higher than Cristallo et al. (2011) and Karakas (2010). A higher  $^{12}\text{C}$  enrichment in our models is due to the CBM activated at the bottom of the PDCZ. The consistent amount of ejected  $^{12}\text{C}$  with

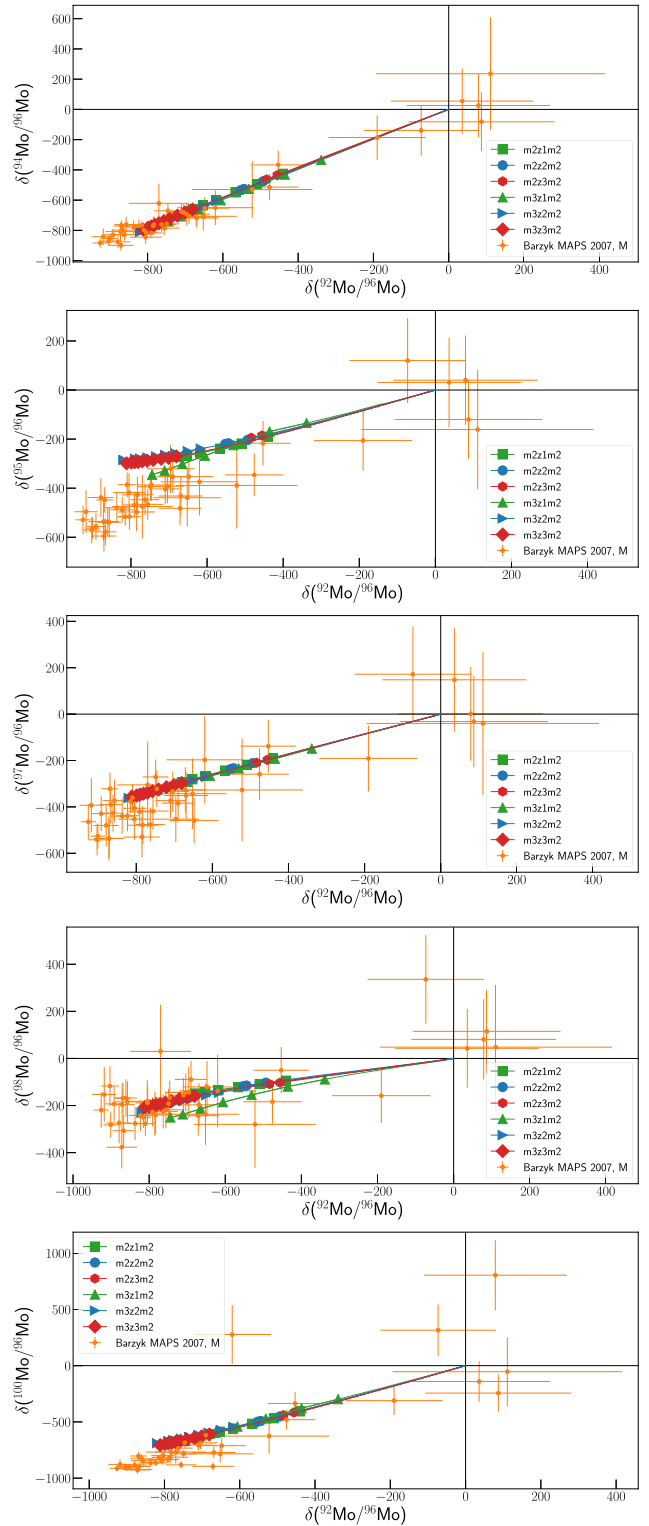


**Figure 25.** Comparison of stellar models presented in this work with Barzyk et al. (2007) measurements of Mo isotopic ratios.

RI18 is a consequence of the same CBM scheme adopted at the bottom of the intershell. The  $^{14}\text{N}$  yields are consistent within 20 per cent. Concerning  $^{16}\text{O}$ ,  $m3z2m2$  show a larger production, up to 60 per cent compared to Cristallo et al. (2011) and Karakas (2010), while it is consistent with RI18. As for  $^{12}\text{C}$ , this higher

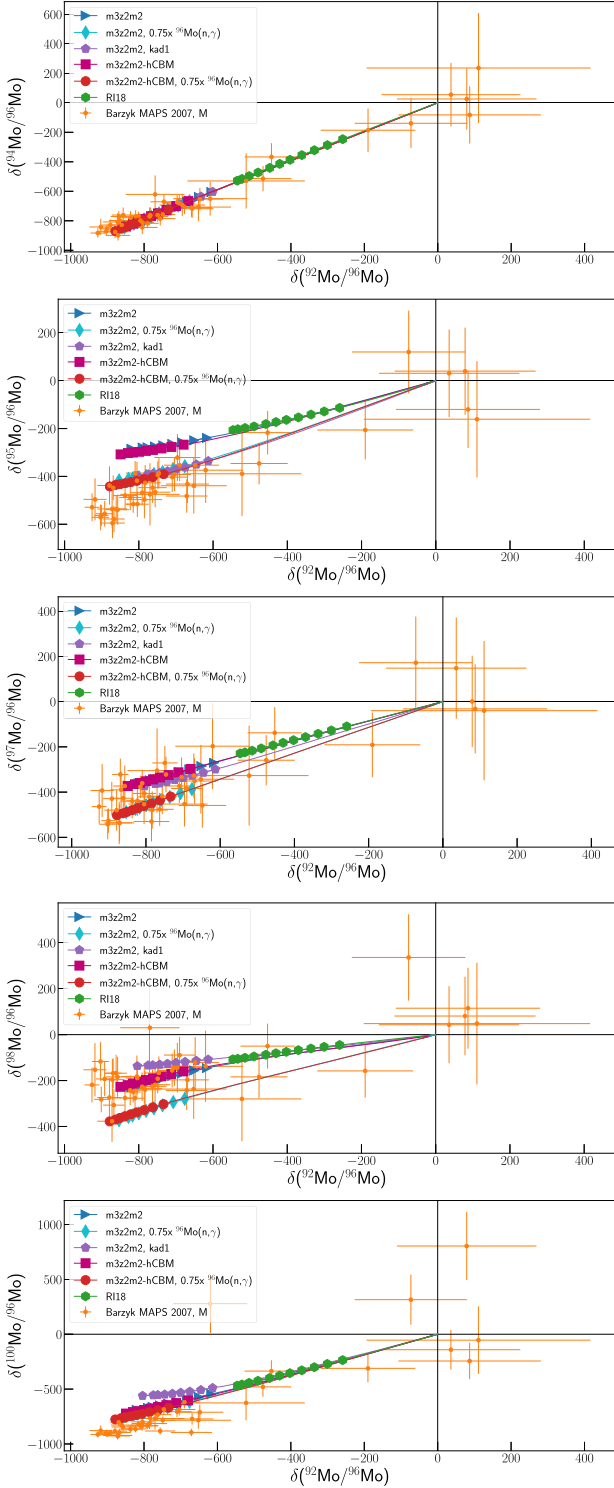


**Figure 26.** Predictions from m3z2m2 model calculated with Kadonis 0.3, Kadonis 1.0, and Kadonis 0.3 with the  $^{96}\text{Mo}(n,\gamma)^{97}\text{Mo}$  set to its lower limit (i.e. multiplied by a factor 0.75).

production corresponds to the CBM scheme we applied during the TP, that both Cristallo et al. (2011) and Karakas (2010) do not include. Concerning the *s*-process nucleosynthesis, the final ejected masses from m3z2m2 of  $^{88}\text{Sr}$ ,  $^{138}\text{Ba}$ , and  $^{208}\text{Pb}$  are  $3.34 \times 10^{-7}$ ,  $1.96 \times 10^{-7}$ , and  $3.28 \times 10^{-8} M_{\odot}$ , respectively.

**Table 5.** List of the reaction rates with the highest impact on the observables we considered in this work. Also the most affected isotope by each reaction is shown. For neutron-capture rates, we add the classification and the main nuclide affected given by Cescutti et al. (2018).

Reaction rate	Affected observable	Cescutti et al. (2018) classification
$^{137}\text{Ba}(n,\gamma)^{138}\text{Ba}$	$^{137}\text{Ba}/^{136}\text{Ba}$	Level 1 for $^{137}\text{Ba}$
$^{95}\text{Mo}(n,\gamma)^{96}\text{Mo}$	$^{95}\text{Mo}/^{96}\text{Mo}$	Level 1 for $^{95}\text{Mo}$
$^{96}\text{Mo}(n,\gamma)^{97}\text{Mo}$	$^{94}, ^{95}, ^{97}, ^{98}, ^{100}\text{Mo}/^{96}\text{Mo}$	Level 1 for $^{96}\text{Mo}$
$^{94}\text{Zr}(n,\gamma)^{95}\text{Zr}$	$^{90}, ^{91}, ^{92}, ^{96}\text{Zr}/^{94}\text{Zr}$	Level 1 for $^{96}\text{Zr}$
$^{95}\text{Zr}(n,\gamma)^{96}\text{Zr}$	$^{96}\text{Zr}/^{94}\text{Zr}$	Level 2 for $^{96}\text{Zr}$
$^{22}\text{Ne}(\alpha,n)^{25}\text{Mg}$	$^{96}\text{Zr}/^{94}\text{Zr}$	–

Cristallo et al. (2011) predict a much higher production of  $^{88}\text{Sr}$ , which is  $1.63 \times 10^{-6} M_{\odot}$ , due to the smaller  $^{13}\text{C}$ -pockets obtained in our models. On the other hand, the calculated ejected amount of  $^{138}\text{Ba}$  and  $^{208}\text{Pb}$  are consistent with our results being  $1.69 \times 10^{-7}$  and  $4.82 \times 10^{-8} M_{\odot}$ , respectively, which is explained by the higher neutron exposure of our models originating from the higher  $^{12}\text{C}$  enrichment in the intershell.

RI18 predict on average a factor of two lower production, with  $1.98 \times 10^{-7}$ ,  $7.58 \times 10^{-8}$ , and  $2.24 \times 10^{-8} M_{\odot}$  of  $^{88}\text{Sr}$ ,  $^{138}\text{Ba}$ , and  $^{208}\text{Pb}$ , respectively. This is due to the  $^{13}\text{C}$ -pockets being between two and three times larger in our models compared to RI18, but with the same peak abundance of  $^{13}\text{C}$  in them which give similar [hs/l<sub>s</sub>] values, again because of the same CBM scheme adopted at the bottom of the intershell.

A final important aspect is the different mass-loss rates prescriptions used during the AGB phase in different works. In particular, in this work and in RI18 the prescription from Bloeker (1995) was adopted, while both Cristallo et al. (2011) and Karakas (2010) used the Vassiliadis & Wood (1993) mass-loss prescription. Stancliffe & Jeffery (2007) discussed the effect of varying the mass-loss on the evolution and nucleosynthesis of a  $1.5 M_{\odot}$ ,  $Z = 0.008$  model. They found that when switching between Bloeker (1995) and Vassiliadis & Wood (1993) mass-loss prescriptions, the total ejected yields of most of the elements considered were consistent within a factor of two. This reasonably quantifies the sensitivity of our results with respect to changes in the mass-loss rate.

## 5 CONCLUSIONS

In this work we presented a significant update of low-mass AGB star models and nucleosynthesis calculations presented in RI18. In that work, the *s*-process production was low compared to observations. We tackled this by re-calculating the low-mass AGB models with the same stellar code, general input physics parameters with the difference being describing the convective boundaries during TDU events according to the scheme described by Battino et al. (2016), which was based on the IGW-mixing scenario described by Denissenkov & Tout (2003). The direct consequence of this is a  $^{13}\text{C}$ -pocket up to three times larger in mass coordinate than in RI18, with the final *s*-process production increasing by almost a factor of three and now in much better agreement with observations. One additional difference compared to RI18 is the inclusion of the additional metallicity  $Z = 0.03$ , since its contribution to dust production and hence pre-solar grains can be very significant (Lugaro et al. 2018). Moreover, we compute two additional models (labelled ‘hCBM’) with metallicities  $Z = 0.02$

**Table 6.** Comparison between the yields in solar masses for  $m_{3z2m2}$  and the yields from Karakas (2010) (Ka10), Cristallo et al. (2011) (Cr11), and RI18 for their model with same initial mass and metallicity.

Isotope	$m_{3z2m2}$	$m_{3z2m2}$ -hCBM	RI18	Cr11	Ka10
C 12	3.4035341E-02	3.43558877e-02	4.448E-02	1.86110E-02	2.0739544E-02
C 13	2.2231664E-04	2.18517069e-04	2.252E-04	2.20200E-04	1.9436399E-04
N 14	7.0151267E-03	6.90119758e-03	7.685E-03	6.64840E-03	5.6565693E-03
N 15	4.4046608e-06	4.25324193e-06	4.207E-06	4.29400E-06	5.0818235E-06
O 16	3.1633632E-02	3.22309748e-02	3.828E-02	1.94360E-02	2.1144016E-02
O 17	6.2956708e-05	6.20965699e-05	5.194E-05	7.91850E-05	5.5763638E-05
O 18	3.4374702e-05	3.34363411e-05	3.364E-05	3.12110E-05	3.6596495E-05
F 19	4.9649986e-06	4.92340864e-06	7.655E-06	3.68770E-06	4.3487280E-06
NE 20	4.2225594E-03	4.13259733e-03	4.356E-03	3.63520E-03	3.7571993E-03
NE 21	1.2744558e-05	1.24662448e-05	1.270E-05	9.90460E-06	1.0039988E-05
NE 22	2.7187524E-03	2.82343479e-03	3.937E-03	2.32210E-03	2.1113991E-03
NA 23	1.4976682E-04	1.49833381e-04	1.772E-04	1.87730E-04	1.2845088E-04
MG 24	1.3712457E-03	1.34172081e-03	1.421E-03	1.84710E-03	1.1949923E-03
MG 25	2.9955618E-04	2.92761999e-04	2.915E-04	2.43210E-04	1.6784266E-04
MG 26	4.5746367E-04	4.54130815e-04	4.726E-04	2.88120E-04	1.9374024E-04
AL 27	1.5420979E-04	1.50610193e-04	1.585E-04	2.08100E-04	1.3861095E-04
SI 28	1.7175335E-03	1.67961680e-03	1.770E-03	2.36270E-03	1.5164100E-03
SI 29	9.2162458e-05	9.01472831e-05	9.501E-05	1.24570E-04	7.9920115E-05
SI 30	6.7840128e-05	6.65214218e-05	6.975E-05	8.60130E-05	5.5390818E-05
P 31	1.7451779e-05	1.71499494e-05	1.771E-05	2.28230E-05	1.9017965E-05
S 33	7.9125730e-06	7.74800508e-06	8.331E-06	1.04160E-05	7.6937777E-06
S 34	4.5194069e-05	4.42301243e-05	4.601E-05	5.91400E-05	4.3391171E-04
FE 54	1.8268714E-04	1.78490960e-04	1.874E-04	2.49280E-04	1.6390771E-04
FE 56	3.0096567E-03	2.94198314e-03	3.100E-03	4.08090E-03	2.7071363E-03
FE 57	8.1660429e-05	8.00810684e-05	8.781E-05	1.02140E-04	7.2351380E-05
FE 58	2.9018441e-05	2.90010573e-05	3.211E-05	1.76610E-05	1.1919641E-05
CO 59	1.3762730e-05	1.36096972e-05	1.441E-05	1.33220E-05	8.5931824E-06
NI 58	1.2853806E-04	1.25593342e-04	1.317E-04	1.71330E-04	1.1363259E-04
NI 60	5.5129775e-05	5.40953096e-05	5.698E-05	6.93570E-05	4.5602490E-05
NI 61	3.9916327e-06	3.97199615e-06	4.122E-06	3.46150E-06	8.8770785E-06
NI 62	1.0936648e-05	1.08258788e-05	1.056E-05	1.04870E-05	5.0042019E-08
NI 64	4.0636092e-06	4.02730786e-06	3.165E-06	3.32430E-06	–
SR 88	3.3440015e-07	3.80870156e-07	1.978E-07	1.63060E-06	–
Y 89	9.2306586e-08	1.06181661e-07	5.072E-08	3.17410E-07	–
ZR 90	9.6840845e-08	1.11106954e-07	5.726E-08	3.24600E-07	–
BA136	2.1123224e-08	2.61090422e-08	9.317E-09	2.79920E-08	–
BA138	1.9605483e-07	2.43881700e-07	7.581E-08	1.68590E-07	–
LA139	2.2851196e-08	2.82865328e-08	9.138E-09	2.00170E-08	–
PB208	3.2787968e-08	3.75103148e-08	2.243E-08	4.82470E-08	–

and 0.03 with an increased CBM under the convective envelope during TDUs. This increased CBM efficiency is well inside the uncertainties characterizing the IGW-mixing parameterization of Denissenkov & Tout (2003), and produces a  $^{13}\text{C}$ -pocket about 50 per cent larger compared to when the standard setting is adopted.

We validated our results by comparing them with a large set of observables, including carbon-stars and barium-stars surface abundances inferred from spectroscopy and isotopic ratios from pre-solar grains. We noticed how ‘hCBM’ models, forming a larger  $^{13}\text{C}$ -pocket, generally performs better when compared to observations. This indicates how uncertainties affecting CBM impacts our *s*-process results, motivating us to do a future dedicated study before completing re-computing the whole metallicity grid of RI18. Within all uncertainties (stellar modelling, nuclear physics, and observations) our models agree with most of observational data. The most difficult observables to be reproduced are the full ranges of some isotopic ratios, precisely  $^{84}\text{Sr}/^{86}\text{Sr}$ ,  $^{137}\text{Ba}/^{136}\text{Ba}$ ,  $^{96}\text{Zr}/^{94}\text{Zr}$ ,  $^{95,100}\text{Mo}/^{96}\text{Mo}$ .

We explored the role of rotation-induced mixing adopting a simple parametric approach, confirming it as a strong candidate to explain the range of observed values in pre-solar grains. It is anyway important to notice our assumption about stellar rotation being an efficient extra-mixing source in AGB stars, even though this is actually still a matter of debate (see Herwig 2005; Deheuvels et al. 2015; Straniero et al. 2015).

We confirm results by Lugaro et al. (2018), as our AGB models with metallicity  $Z = 0.03$  provide a better fit with grains. This is in particular visible for  $^{138}\text{Ba}/^{136}\text{Ba}$  ratio. On the other hand, the same result can be obtained by adopting models with lower metallicity and including rotation-induced mixing.

We identified a number of reaction rates that impact our results, some of which already have been classified as key-reaction rate for AGB nucleosynthesis by Cescutti et al. (2018). We therefore want to suggest them as priority candidates for future measurements.

Finally, we provide the final ejected yields from our models that can be used as inputs for galactic chemical evolution simulations. Full tables are available online as described in the text.

## ACKNOWLEDGEMENTS

This research was enabled in part by support provided by WestGrid ([www.westgrid.ca](http://www.westgrid.ca)) and Compute Canada Calcul Canada ([www.computeCanada.ca](http://www.computeCanada.ca)). NuGrid data are served by Canfar CADC. This work received support from the Science and Technology Facilities Council UK (ST/M006085/1), and the European Research Council ERC-2015-STG Nr. 677497 and ERC-2016-CO Grant 724560. Part of this work was performed under the auspices of the U.S. Department of Energy by Lawrence Livermore National Laboratory under Contract DE-AC52-07NA27344 and was supported by the LLNL-LDRD Program under Project No. 19-LW-033. LLNL-JRNL-765023. This work used the DiRAC Complexity system, operated by the University of Leicester IT Services, which forms part of the STFC DiRAC HPC Facility ([www.dirac.ac.uk](http://www.dirac.ac.uk)). This equipment is funded by BIS National E-Infrastructure capital grant ST/K000373/1 and STFC DiRAC Operations grant ST/K0003259/1. DiRAC is part of the National E-Infrastructure. RH acknowledges support from the World Premier International Research Centre Initiative (WPI Initiative), MEXT, Japan. This article is based upon work from the ChETEC COST Action (CA16117), supported by COST (European Cooperation in Science and Technology). MP acknowledges significant support to NuGrid from NSF grant PHY-1430152 (JINA Center for the Evolution of the Elements) and STFC (through the University of Hull's Consolidated Grant ST/R000840/1), and access to VIPER, the University of Hull High Performance Computing Facility. MP acknowledges the support from the 'Lendület-2014' Programme of the Hungarian Academy of Sciences (Hungary) and from the BRIDGCE UK network.

## REFERENCES

- Abia C. et al., 2002, *ApJ*, 579, 817  
 Barzyk J. G. et al., 2007, *Meteorit. Planet. Sci.*, 42, 1103  
 Battino U. et al., 2016, *ApJ*, 827, 30  
 Bloeker T., 1995, *A&A*, 297, 727  
 Burbidge E. M., Burbidge G. R., Fowler W. A., Hoyle F., 1957, *Rev. Mod. Phys.*, 29, 547  
 Busso M., Gallino R., Lambert D. L., Travaglio C., Smith V. V., 2001, *ApJ*, 557, 802  
 Cameron A. G. W., 1957, *PASP*, 69, 201  
 Cantiello M., Mankovich C., Bildsten L., Christensen-Dalsgaard J., Paxton B., 2014, *ApJ*, 788, 93  
 Cescutti G., Hirschi R., Nishimura N., Hartogh J. W. den., Rauscher T., Murphy A. S. J., Cristallo S., 2018, *MNRAS*, 478, 4101  
 Cristallo S., Straniero O., Gallino R., Piersanti L., Domínguez I., Lederer M. T., 2009, *ApJ*, 696, 797  
 Cristallo S. et al., 2011, *ApJS*, 197, 17  
 Cseh B. et al., 2018, *A&A*, 620, A146  
 Deheuvels S., Ballot J., Beck P. G., Mosser B., Østensen R., García R. A., Goupil M. J., 2015, *A&A*, 580, A96  
 Denissenkov P. A., Tout C. A., 2003, *MNRAS*, 340, 722  
 Ferrarotti A. S., Gail H.-P., 2006, *A&A*, 447, 553  
 Freytag B., Ludwig H.-G., Steffen M., 1996, *A&A*, 313, 497  
 Gallino R., Arlandini C., Busso M., Lugaro M., Travaglio C., Straniero O., Chieffi A., Limongi M., 1998, *ApJ*, 497, 388  
 Grevesse N., Noels A., 1993, in Prantzos N., Vangioni-Flam E., Casse M., eds, *Origin and Evolution of the Elements*, Astronomisches Rechen-Institut, Heidelberg, p. 15  
 Herwig F., 2000, *A&A*, 360, 952  
 Herwig F., 2005, *ARA&A*, 43, 435  
 Herwig F., Bloeker T., Schoenberner D., El Eid M., 1997, *A&A*, 324, L81  
 Herwig F., Langer N., Lugaro M., 2003, *ApJ*, 593, 1056  
 Herwig F., Freytag B., Fuchs T., Hansen J. P., Hueckstaedt R. M., Porter D. H., Timmes F. X., Woodward P. R., 2007, in Kerschbaum F., Charbonnel C., Wing R. F., eds, *ASP Conf. Ser. Vol. 378, Why Galaxies Care About AGB Stars: Their Importance as Actors and Probes*. Astron. Soc. Pac., San Francisco, p. 43  
 Herwig F. et al., 2008, in *Proceedings of Science*, 023, 10th Symposium on Nuclei in the Cosmos, July 27 - August 1 2008. Mackinac Island, Michigan, USA  
 Iliadis C., Longland R., Champagne A. E., Coc A., Fitzgerald R., 2010, *Nucl. Phys. A*, 841, 31  
 Jaeger M., Kunz R., Mayer A., Hammer J. W., Staudt G., Kratz K. L., Pfeiffer B., 2001, *Phys. Rev. Lett.*, 87, 202501  
 Kalirai J. S., Marigo P., Tremblay P.-E., 2014, *ApJ*, 782, 17  
 Käppeler F., Gallino R., Bisterzo S., Aoki W., 2011, *Rev. Mod. Phys.*, 83, 157  
 Karakas A., Lattanzio J. C., 2007, *Publ. Astron. Soc. Aust.*, 24, 103  
 Karakas A. I., 2010, *MNRAS*, 403, 1413  
 Karakas A. I., Lugaro M., 2016, *ApJ*, 825, 26  
 Kippenhahn R., Weigert A., 1990, *Stellar Structure and Evolution*. Springer, Berlin  
 Langer N., Heger A., Wellstein S., Herwig F., 1999, *A&A*, 346, L37  
 Liu N., Gallino R., Bisterzo S., Davis A. M., Savina M. R., Pellin M. J., 2014, *ApJ*, 788, 163  
 Liu N. et al., 2015, *ApJ*, 803, 12  
 Lugaro M., Herwig F., Lattanzio J. C., Gallino R., Straniero O., 2003a, *ApJ*, 586, 1305  
 Lugaro M., Davis A. M., Gallino R., Pellin M. J., Straniero O., Käppeler F., 2003b, *ApJ*, 593, 486  
 Lugaro M., Tagliente G., Karakas A. I., Milazzo P. M., Käppeler F., Davis A. M., Savina M. R., 2014, *ApJ*, 780, 95  
 Lugaro M., Karakas A. I., Pető M., Plachy E., 2018, *Geochim. Cosmochim. Acta*, 221, 6  
 Maeder A., Meynet G., 2000, *ARA&A*, 38, 143  
 Marigo P., 2002, *A&A*, 387, 507  
 Marigo P., 2012, in Manchado A., Stanghellini L., Schönberner D., eds, *IAU Symposium, Planetary Nebulae: An Eye to the Future*, Puerto Cruz, Tenerife (Spain), p. 87  
 Marigo P., Girardi L., 2007, *A&A*, 469, 239  
 Mathis S., Palacios A., Zahn J.-P., 2004, *A&A*, 425, 243  
 Mattsson L., Wahlin R., Höfner S., 2010, *A&A*, 509, A14  
 Nanni A., Bressan A., Marigo P., Girardi L., 2013, *MNRAS*, 434, 2390  
 Nanni A., Marigo P., Girardi L., Rubele S., Bressan A., Groenewegen M. A. T., Pastorelli G., Aringer B., 2018, *MNRAS*, 473, 5492  
 Nucci M. C., Busso M., 2014, *ApJ*, 787, 141  
 Paczyński B., 1970, *Acta Astron.*, 20, 47  
 Paxton B., Bildsten L., Aaron D., Herwig F., Lesaffre P., Timmes F., 2010, *ApJS*, 192, 3  
 Pereira C. B., Sales Silva J. V., Chavero C., Roig F., Jilinski E., 2011, *A&A*, 533, A51  
 Piersanti L., Cristallo S., Straniero O., 2013, *ApJ*, 774, 98  
 Pignatari M. et al., 2016, *ApJS*, 225, 24  
 Raut R. et al., 2013, *Phys. Rev. Lett.*, 111, 112501  
 Ritter C., Herwig F., Jones S., Pignatari M., Fryer C., Hirschi R., 2018, *MNRAS*, 480, 538  
 Siess L., Goriely S., Langer N., 2004, *A&A*, 415, 1089  
 Stancliffe R. J., Jeffery C. S., 2007, *MNRAS*, 375, 1280  
 Straniero O., Gallino R., Busso M., Chieffi A., Raiteri C. M., Limongi M., Salari M., 1995, *ApJ*, 440, L85  
 Straniero O., Gallino R., Cristallo S., 2006, *Nucl. Phys. A*, 777, 311  
 Straniero O., Cristallo S., Piersanti L., 2015, in Kerschbaum F., Wing R. F., Hron J., eds, *ASP Conf. Ser. Vol. 497, Why Galaxies Care about AGB Stars III: A Closer Look in Space and Time*. Astron. Soc. Pac., San Francisco, p. 259  
 Tagliente G., Lugaro M., Karakas A. I., Milazzo P. M., n TOF Collaboration, 2012, in *Proceedings of Science*, 025., 12th Symposium on Nuclei in the Cosmos, August 5 - 12 2012, Cairns, Australia  
 Trippella O., Busso M., Palmerini S., Maiorca E., Nucci M. C., 2016, *ApJ*, 818, 125

Vassiliadis E., Wood P. R., 1993, *ApJ*, 413, 641  
Werner K., Herwig F., 2006, *PASP*, 118, 183  
Zahn J.-P., 1992, *A&A*, 265, 115  
Zamora O., Abia C., Plez B., Domínguez I., Cristallo S., 2009, *A&A*, 508, 909

## SUPPORTING INFORMATION

Supplementary data are available at [MNRAS](#) online.

**NuGrid\_Yields\_all.txt**

Please note: Oxford University Press is not responsible for the content or functionality of any supporting materials supplied by the authors. Any queries (other than missing material) should be directed to the corresponding author for the article.

This paper has been typeset from a  $\text{T}_{\text{E}}\text{X}/\text{L}_{\text{A}}\text{T}_{\text{E}}\text{X}$  file prepared by the author.